The Astrophysical Journal, 811:76 (23pp), 2015 October 1 doi:10.1088/0004-637X/811/2/76

HUBBLE TARANTULA TREASURY PROJECT. II. THE STAR-FORMATION HISTORY OF THE STARBURST REGION NGC 2070 IN 30 DORADUS*

M. Cignoni[1], E. Sabbi[1], R. P. van der Marel[1], M. Tosi[2], D. Zaritsky[3], J. Anderson[1], D. J. Lennon[4], A. Aloisi[1], G. de Marchi[5], D. A. Gouliermis[6], E. K. Grebel[7], L. J. Smith[8], and P. Zeidler[7]

[1] Space Telescope Science Institute, 3700 San Martin Drive, Baltimore, MD, 21218, USA; cignoni@stsci.edu
[2] Istituto Nazionale di Astrofisica, Osservatorio Astronomico di Bologna, Via Ranzani 1, I-40127 Bologna, Italy
[3] Steward Observatory, University of Arizona, 933 North Cherry Avenue, Tucson, AZ 85721, USA
[4] ESA—European Space Astronomy Center, Apdo. de Correo 78, E-28691 Villanueva de la Cañada, Madrid, Spain
[5] Space Science Department, European Space Agency, Keplerlaan 1, 2200 AG Noordwijk, The Netherlands
[6] Universität Heidelberg, Zentrum für Astronomie, Institut für Theoretische Astrophysik, Albert-Ueberle-Str. 2, D-69120 Heidelberg, Germany
[7] Astronomisches Rechen-Institut, Zentrum für Astronomie der Universität Heidelberg, Mönchhofstr. 12–14, D-69120 Heidelberg, Germany
[8] ESA/STScI, 3700 San Martin Drive, Baltimore, MD 21218, USA

Received 2015 May 16; accepted 2015 August 4; published 2015 September 24

ABSTRACT

We present a study of the recent star formation (SF) of 30 Doradus in the Large Magellanic Cloud (LMC) using the panchromatic imaging survey Hubble Tarantula Treasury Project. In this paper we focus on the stars within 20 pc of the center of 30 Doradus, the starburst region NGC 2070. We recovered the SF history by comparing deep optical and near-infrared color–magnitude diagrams (CMDs) with state-of-the-art synthetic CMDs generated with the latest PAdova and TRieste Stellar Evolution Code (PARSEC) models, which include all stellar phases from pre-main-sequence to post-main-sequence. For the first time in this region we are able to measure the SF using intermediate- and low-mass stars simultaneously. Our results suggest that NGC 2070 experienced prolonged activity. In particular, we find that the SF in the region (1) exceeded the average LMC rate ≈ 20 Myr ago, (2) accelerated dramatically ≈ 7 Myr ago, and (3) reached a peak value 1–3 Myr ago. We did not find significant deviations from a Kroupa initial mass function down to 0.5 $M_\odot$. The average internal reddening $E(B - V)$ is found to be between 0.3 and 0.4 mag.

Key words: galaxies: star clusters: individual (30 Doradus, NGC 2070) – Hertzsprung–Russell and C–M diagrams – Magellanic Clouds – stars: formation – stars: pre-main sequence

1. INTRODUCTION

The Large Magellanic Cloud (LMC) harbors the nearest giant extragalactic H ii region (Kennicutt 1991, p. 139), the Tarantula Nebula (30 Doradus). The central area of the nebula is dominated by the star-forming region NGC 2070, a collective of several dense subclusters (Walborn & Blades 1997; Sabbi et al. 2012) whose light is dominated by massive OB stars. The most prominent and central of these subclusters is the bound super star cluster (SSC) R136.

The whole 30 Doradus region (~200 pc) has a number of characteristics that make it extraordinary. First of all, it displays an extreme rate of star formation (SF), enclosing one-quarter of the total massive recent (<10 Myr) SF in the LMC (Kennicutt 1991, p. 139). Its dense center, R136, with at least $2.2 \times 10^4\,M_\odot$ within a radius of 4.7 pc (Hunter et al. 1995), can be classified as a relatively low-mass clone of more distant starburst clusters, likely building blocks of starburst galaxies.

Due to the proximity of the LMC, 30 Doradus can be imaged with the *Hubble Space Telescope* (*HST*) on scales down to ~0.01 pc, resolving stars down to the subsolar regime. By coupling *HST* imaging with ground-based spectroscopy diagnostics, we know that the region has undergone continuous SF activity or a superposition of multiple bursts of SF. Indeed, over the whole region, there is evidence of at least three events: (1) an ongoing off-center activity, as documented by the presence of embedded O-type stars and luminous infrared protostars along an arc of molecular gas and warm dust around 30 Doradus (Hyland et al. 1992; Rubio et al. 1992, 1998; Walborn & Blades 1997; Walborn et al. 1999; Brandner et al. 2001); (2) a recent event, represented by the SSC R136 itself, 2 Myr old or less, as inferred from spectroscopy of the O stars (Massey & Hunter 1998), 3–4 Myr old from *HST* imaging (Hunter et al. 1995); and (3) an "old" event, documented by the presence of Hodge 301, a 25 Myr old cluster (Grebel & Chu 2000) located only 3 arcmin northwest of R136.

However, most high-resolution studies are limited to a few bands and cover only small patches of the 30 Doradus complex. The Hubble Tarantula Treasury Project (HTTP; Sabbi et al. 2015), an *HST* survey covering a $\sim 14' \times 12'$ wide area around 30 Doradus at high resolution, fills this gap. This unique data set, which combines resolution and spatial coverage, can be exploited in varied ways, including studies of massive SF, low-mass SF, the initial mass function (IMF), and the reddening distribution. In our current paper, we take the opportunity to explore the SF during the last 50 Myr for the central 40 pc of 30 Doradus, a.k.a. the starburst region NGC 2070, by comparing the observational color–magnitude diagrams (CMDs) with state-of-the-art synthetic CMDs. These simulations incorporate the latest (V.1.2S) set of PAdova and TRieste Stellar Evolution Code (PARSEC) isochrones (see Bressan et al. 2012 and Tang et al. 2014), the first theoretical library to include homogeneously all stellar phases from pre-main-sequence (PMS) to post-main-sequence for all masses between 0.1 and 350 $M_\odot$. For the first time, we derive the history of the region using low- and intermediate-mass stars, either in the PMS or main sequence (MS) phases,

* Based on observations with the NASA/ESA *Hubble Space Telescope*, obtained at the Space Telescope Science Institute, which is operated by AURA Inc., under NASA contract NAS 5-26555.

simultaneously. In particular, we exploit magnitudes and colors of the PMS turn-ons (hereafter TOn; see Section 3), that is, the CMD loci where the PMS phase joins the MS. This "hook" has been demonstrated to be particularly sensitive to age (see, e.g., Stauffer 1980; Belikov et al. 1998; Baume et al. 2003; Stolte et al. 2004; Cignoni et al. 2010; Mayne 2010). We use both the optical F555W versus F555W−F775W and the near-infrared (NIR) F110W versus F110W−F160W CMDs of the HTTP sample, which offer complementary advantages in terms of higher spatial resolution (the optical) and lower reddening sensitivity (the NIR).

To recover the SF rate of NGC 2070 since the beginning of its activity, there are three important factors that must be accounted for: differential reddening, LMC field contamination, and stellar crowding. The first causes the CMD features to appear redder and more scattered, mimicking older populations and lowering the age resolution. Field contamination mostly adds low-mass stars to the sample, mimicking much older populations and a steeper IMF. Finally, stellar confusion affects completeness and, therefore, the reachable look-back time. Moreover, unaccounted incompleteness can also mimic mass segregation.

This paper is the second of a series aimed at exploiting the HTTP sample. In the first paper we presented the main goals of the survey (Sabbi et al. 2013). In the next papers we will release the final HTTP catalog (Sabbi et al. 2015, submitted), and we will investigate the SF history (SFH) of the other two important star-forming regions or clusters of 30 Doradus, Hodge 301 and NGC 2060, and the mass functions and possible mass segregation in various 30 Doradus clusters.

The paper is structured as follows. In Section 2 we briefly describe the observations. Section 3 is dedicated to the physics of the TOn clock. In Section 4 we identify the general properties of the stellar populations in the HTTP data set, with special emphasis on NGC 2070. In Section 5 we perform artificial star tests, the only way to take crowding into account, and we recover the SFH of NGC 2070 using the synthetic CMD approach. Field contamination is also carefully discussed. The results are presented in Section 6 and compared to the literature in Section 7. Section 8 compares NGC 2070 with other starburst regions. Our conclusions (Section 9) close the paper.

Throughout the paper, for the sake of simplicity, we will refer to the entire HTTP data set as "30 Doradus," the central ionizing region as NGC 2070, and its core as R136.

2. OBSERVATIONS AND PHOTOMETRIC REDUCTION

We observed 30 Doradus with the *HST* Wide-field Camera 3 (WFC3) and the *HST* Advanced Camera for Surveys (ACS) as part of proposal GO-12939 (PI: E. Sabbi). We built this program on an existing *HST* monochromatic survey in the F775W filter (GO-12499, PI: Lennon), designed to measure proper motions of runaway candidates. In both data sets we used the Wide-field Channel (WFC) of ACS in parallel with either the UVIS or the IR channels of WFC3 to maximize the efficiency of the observations. The images were taken with the filters F275W, F336W, F555W, F658N, F110W, and F160W between 2012 December and 2013 September. The survey utilized 60 orbits. Figure 1 shows the F775W image of 30 Doradus with the major stellar concentrations indicated, NGC 2070, Hodge 301, and NGC 2060.

Bright and faint sources are respectively identified using the packages `img2xym_WFC.09x10` (Anderson & King 2006) and KS2, an evolution of the program described in Anderson et al. (2008). A detailed description of the photometric analysis can be found in Sabbi et al. (2015, submitted).

We culled the catalog of detected objects to only include sources with high quality in the point spread function (PSF) fitting, $Q_{\rm fit} > 0.75$. The final catalog contains ~30,000 stars detected in the filter F275W, ~100,000 in F336W, ~400,000 in F555W, ~130,000 in F658N, ~620,000 in F775W, 520,000 in F110W, and 570,000 in the F160W.

3. STELLAR CLOCKS: MS TURN-OFF AND PMS TURN-ON

One of the characteristics of 30 Doradus that makes it a particularly interesting object is the high concentration of massive stars that coexist with a plethora of coeval intermediate- and low-mass PMS stars. This enables us to reconstruct the past history of 30 Doradus using the MS turn-off (MSTO)[9], the locus of the CMD where MS stars exhaust their core hydrogen, and the PMS TOn, where low- and intermediate-mass PMS stars ignite hydrogen in their cores. In terms of stellar mass, the MSTO mass is the mass of the most massive star still on the MS at an evolutionary time corresponding to the age of the cluster, while the TOn mass is the mass of the least massive star that has reached the MS at the age of the cluster. In the following we discuss pros and cons of the two clocks.

Massive stars: The main appeal of using the MSTO of massive stars ($M > 8\,M_\odot$) stems from the high luminosity of such sources, which translates into high-quality photometry and complete samples. The optical and infrared spectra of these objects are well approximated by the Rayleigh–Jeans tail of a blackbody with temperature $T_{\rm eff}$. Hence, given that the spectral energy distribution shape is almost unchanged as a function of wavelength, the optical and infrared colors are nearly constant (and around 0 mag). This is clearly visible in Figure 2, where we overlaid young isochrones of different ages (0.5, 1, 3, 7, 15 Myr) onto the entire HTTP catalog (shaded gray area) in the UV (left panel), optical (middle panel), and NIR (right panel) CMDs. The adopted distance modulus $(m-M)_0$ and reddening $E(B-V)$ are 18.5 (Panagia et al. 1991; Schaefer 2008; Pietrzyński et al. 2013) and 0.3,[10] respectively. The reddening value was chosen by eye to match the average color of the optical upper MS (UMS), whose large dispersion is due to the simultaneous presence of field stars, with average reddening as low as the foreground Milky Way (MW) reddening ($E(B-V) = 0.07$; Fitzpatrick & Savage 1984) and genuine young 30 Doradus stars, with reddening $E(B-V) = 0.3$ or higher (a similar result is found by Doran et al. 2013 and Maíz Apellániz et al. 2014 using OB stars; see also further in this paper). In the NIR CMD, the UMS looks like a vertical line, and isochrones of different age have MSTOs almost indistinguishable from one another. This degeneracy is attenuated in the optical and almost lifted in the UV CMD. Observationally, studies of

[9] Although the term MSTO refers to the end of the MS phase for stars of any mass, the reference here is to stars more massive than $8\,M_\odot$, whose MS evolutionary times are shorter than ≈50 Myr.

[10] For the optical and NIR filters we used the extinction coefficients from De Marchi & Panagia (2014). For the F275W and F336W filters we followed the prescription of De Marchi & Panagia (2014), adding 1.5 to the Fitzpatrick & Massa (1999) law (obtaining $R_{\rm F275W} = 7.62$ and $R_{\rm F336W} = 6.56$).

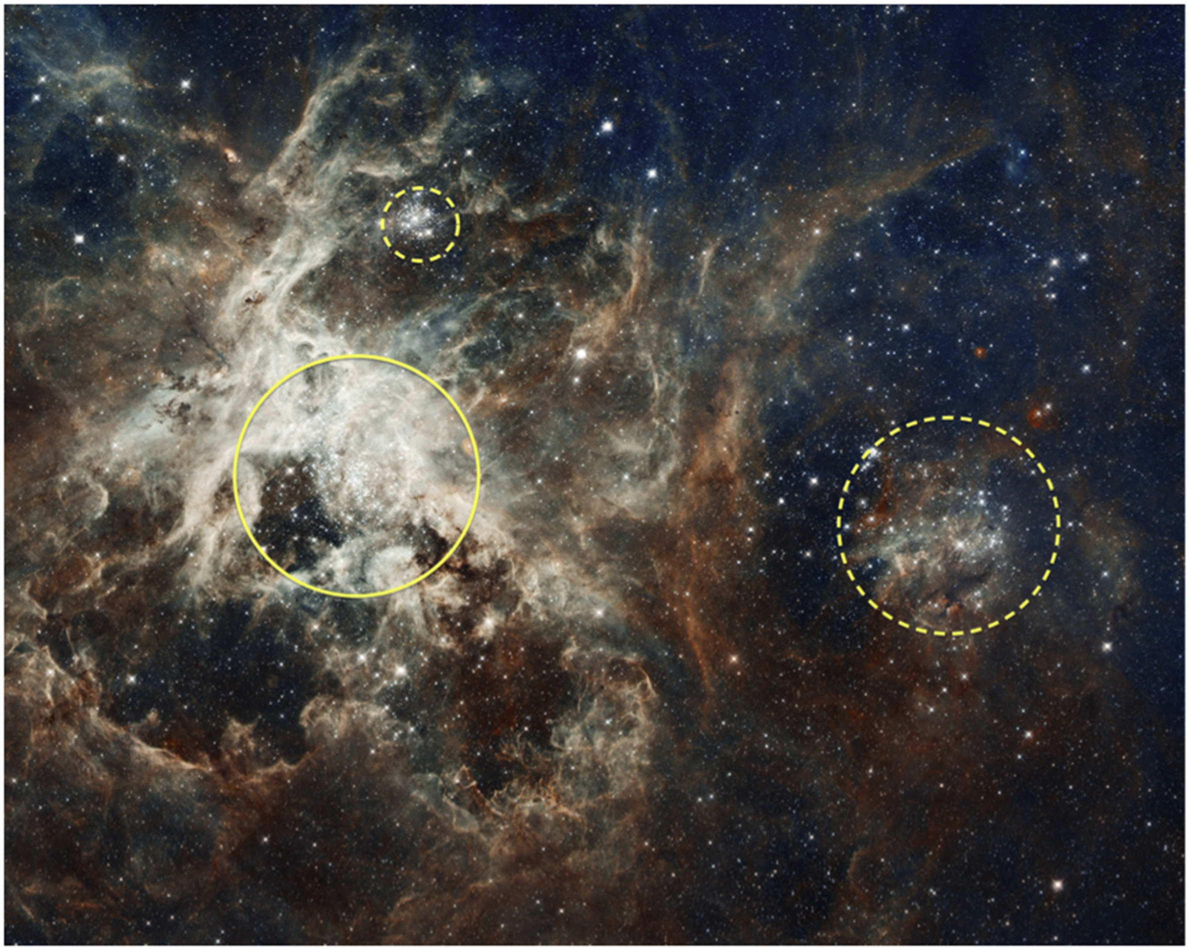

Figure 1. Color composite image of 30 Doradus in F775W (ACS/WFC3 *HST*), O III/8 (ESO 2.2 m, WFI), and H-α/7 (ESO 2.2 m, WFI). The stellar concentrations of NGC 2070 (continuous-line circle), Hodge 301 (dashed small circle), and NGC 2060 (dashed large circle) are also indicated.

massive stars has always been hampered by their rarity, due to the short timescales involved in their evolution and the steepness of the IMF.

On the theoretical side, models of massive stars are still affected by major uncertainties. In particular, physical mechanisms like mass loss, rotation, and binary evolution are not well understood (see, e.g., de Mink et al. 2012).

Intermediate- and low-mass stars: For ages younger than 20–30 Myr, the PMS TOn is another valuable stellar chronometer, which involves intermediate- and low-mass stars instead of massive stars.[11] In analogy with the MSTO, the TOn properties are directly related to the age of the stellar population, but with evolutionary times much shorter than the corresponding MS times. In fact, the age of a cluster is equal to the time spent in the PMS phase by its most massive star still in the PMS phase. By definition, this star is at the TOn. Hence, when the intrinsic luminosity of the TOn is detected, it is straightforward to associate it with the age of the cluster. From the CMD point of view, the potential strength of the TOn is apparent from the morphology of the isochrones in Figure 2. In the optical and NIR CMDs, the isochrone portion just before the MS has a hook and then is significantly flatter than the MS. The TOn is at the vertex of the hook, quite easy to recognize. For ages older than 20−30 Myr, the PMS phase is much closer to the MS and the TOn visibility declines. Theory also predicts that the PMS phase (recognizable as the portion of the isochrones at the right of the MS in Figure 2) itself is a valuable age indicator: older PMS isochrones are fainter and closer to the MS than are younger ones. However, poorly understood phenomena like residual mass accretion and magnetic fields (whose interplay is responsible for the appearing of irregular photometric variability and UV-to-infrared excesses) and observational uncertainties like differential reddening from the circumstellar material can dislocate these stars (especially in the first few megayears) from their theoretical positions in the CMD (see Gouliermis 2012 for a review).

An advantage of the TOn with respect to the MSTO derives from the evolution at nearly constant luminosity of PMS stars near the MS, corresponding to an almost horizontal track in the optical and NIR CMDs. This leads to a luminosity (TOn)–age relation. On the other hand, the MS evolution of massive stars near the MSTO is rather vertical (except in the UV CMD), so age is not uniquely related to luminosity. Among the drawbacks, the intrinsic faintness of TOns compared to the MSTOs makes TOns prone to photometric errors and incompleteness, issues that are exacerbated in the UV CMD because older TOns tend to be also redder. From the theoretical side, the TOn visibility is intimately connected with the PMS evolutionary times, which are still model dependent (see, e.g.,

[11] Stars more massive than 6–7 $M_\odot$ have no PMS phase at all.

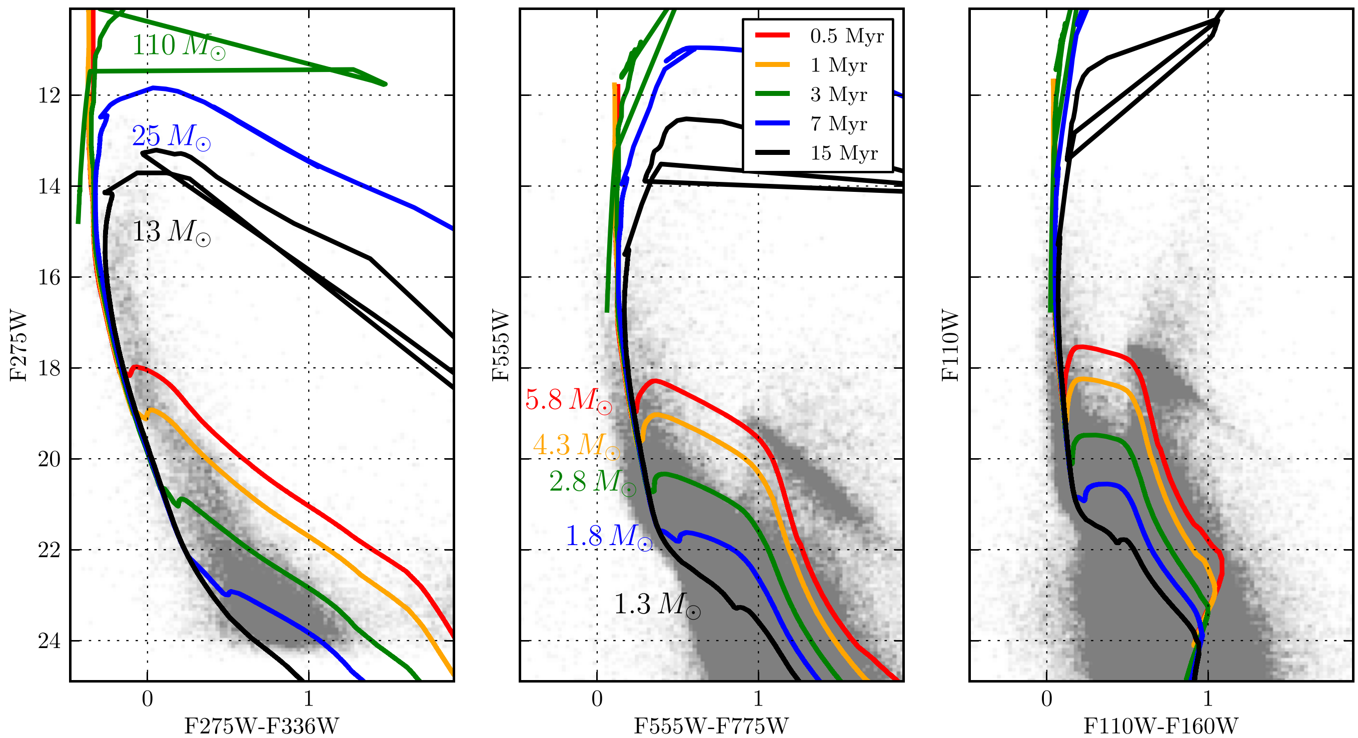

Figure 2. Stellar isochrones of the labeled ages superimposed on the entire HTTP data set in the UV (left panel), optical (middle panel), and NIR (right panel) CMDs. MSTO and TOn masses (at the age of the corresponding isochrones) are also indicated in the UV and optical CMD, respectively. The adopted distance modulus $(m-M)_0$ is 18.5, and $E(B-V)=0.3$.

Baraffe et al. 2009; Hosokawa et al. 2011; Soderblom et al. 2014, p. 219 and references therein).

In this paper we aim to study the SFH of 30 Doradus with the TOns, so we focus our analysis on the optical and NIR CMDs. As shown in the optical CMD (middle panel of Figure 2), the most massive star that is relevant to this study is around 6 $M_\odot$.

The next section is dedicated to a cursory CMD inspection of the stellar populations in the whole HTTP data set.

4. STELLAR POPULATIONS IN THE HTTP CATALOG

The CMD is the most powerful tool to recover the history of a resolved stellar population because different parts of the CMD are populated by different masses with different evolutionary times. In the following analysis, we use the CMD to investigate which populations are present in the whole HTTP catalog and the role of the NGC 2070 region. For this task we use the optical CMD, which offers better spatial resolution than the NIR one. A more quantitative analysis will be the subject of Section 5.

4.1. The Whole HTTP Sample

The F555W versus F555W−F775W CMD of the entire HTTP data set is shown in Figure 3, with overlaid isodensity contours (left panel) and stellar isochrones (PARSEC) of different ages (right panel). The first remarkable feature of this CMD is an extended UMS, populated by a plethora of intermediate- and high-mass stars. As the overlaid isochrones show, the width of the UMS is hardly explained by a difference in age. Moreover, given the average youth of these stars, plausibly much younger than 50 Myr, a metallicity spread is unlikely. As widely discussed in other works (see, e.g., Selman et al. 1999; De Marchi & Panagia 2014; De Marchi et al. 2014), differential reddening is the main cause of this effect, although stellar rotation may also have a role in widening the UMS.

To the right of the UMS, the next striking feature is the very elongated red clump (RC; see also Section 5.1) and a broad red giant branch (RGB). These phases are populated by stars older than 1 Gyr and belonging to the general field population of the LMC. As for the UMS width, most of the elongation and broadening is due to severe differential reddening affecting the region (see Haschke et al. 2011; De Marchi & Panagia 2014; De Marchi et al. 2014).

Finally, the lower MS shows a huge color dispersion (more than 1 mag) at relatively bright magnitudes (F555W $\sim$ 23). As usual, a possible explanation comes from the comparison with the isochrones. Although differential reddening contributes to this effect, pushing part of the lower MS (LMS) to the red, the existence of short-lived massive stars requires that a large fraction of these red stars are genuine PMS stars (coeval with the massive stars).

More information on the nature of these populations can be inferred from their spatial distribution. In fact, the spatial distribution of stars in different evolutionary stages yields important information on the SF processes across the region. Assuming a velocity dispersion of 21–27 km s^{-1} (measured from RGB stars; Carrera et al. 2011), stars older than 1 Gyr are expected to be diffused over scale lengths of several kiloparsecs, so their distribution should be rather uniform over the HTTP field of view (FOV; $\sim$200 pc). On the other hand, stars like those in NGC 2070, young and with low velocity dispersion (4−5 km s^{-1}, as found by Hénault-Brunet et al. 2012 in R136), are expected to be close to their birthplace.

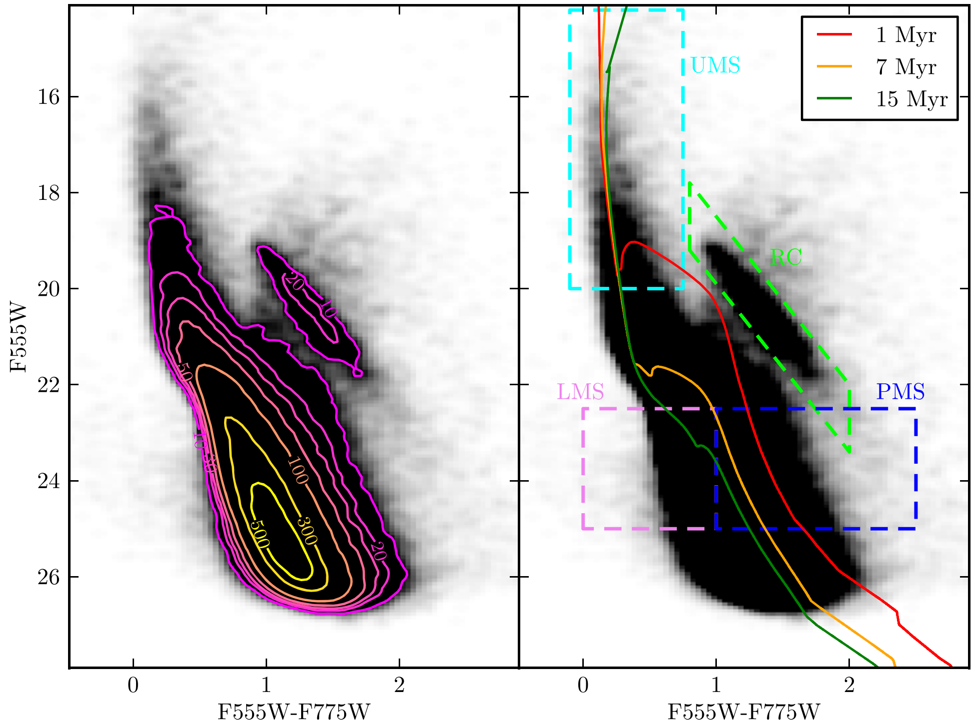

Figure 3. Optical CMD of all stars in the HTTP catalog with overlaid isodensity contours (left panel) and PARSEC isochrones for the labeled ages (distance modulus $(m - M)_0$ and reddening $E(B - V)$ are 18.5 and 0.3, respectively). The dashed selections indicate samples of UMS, LMS, PMS, and RC stars (see text).

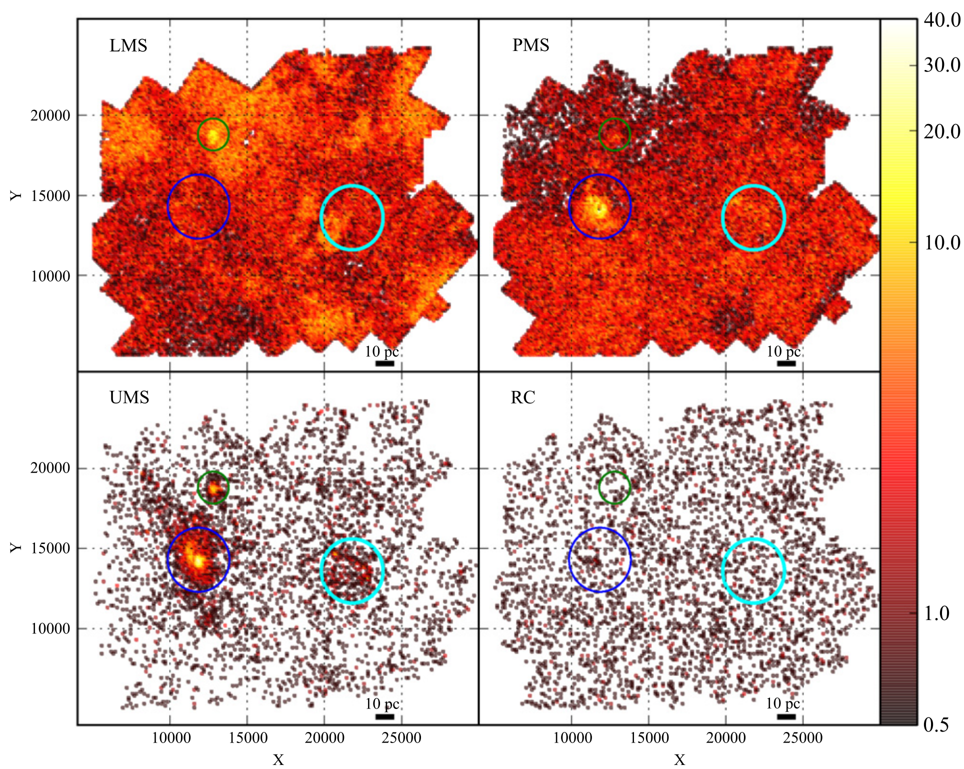

Figure 4. Number of stars per pc^2 (see the color bar on the right in logarithmic units) for different groups of stars (see selection in Figure 3): LMS (top-left panel), PMS (top-right panel), UMS (bottom-left panel), and RC (bottom-right panel) stars. Blue, green, and cyan circles highlight the regions of NGC 2070, Hodge 301, and NGC 2060, respectively.

The right panel of Figure 3 highlights CMD regions of selected UMS (cyan box), RC (green box), low-mass MS (LMS) (pink box), and PMS (blue box) stars. UMS and PMS stars are young objects a few tens of megayears old, RC stars are intermediate-age stars (0.7–2 Gyr), and LMS stars are MS stars older than a few tens of megayears. Figure 4 shows the corresponding spatial density (stars per pc^2). Populations grow more compact as one moves toward younger ages (see also

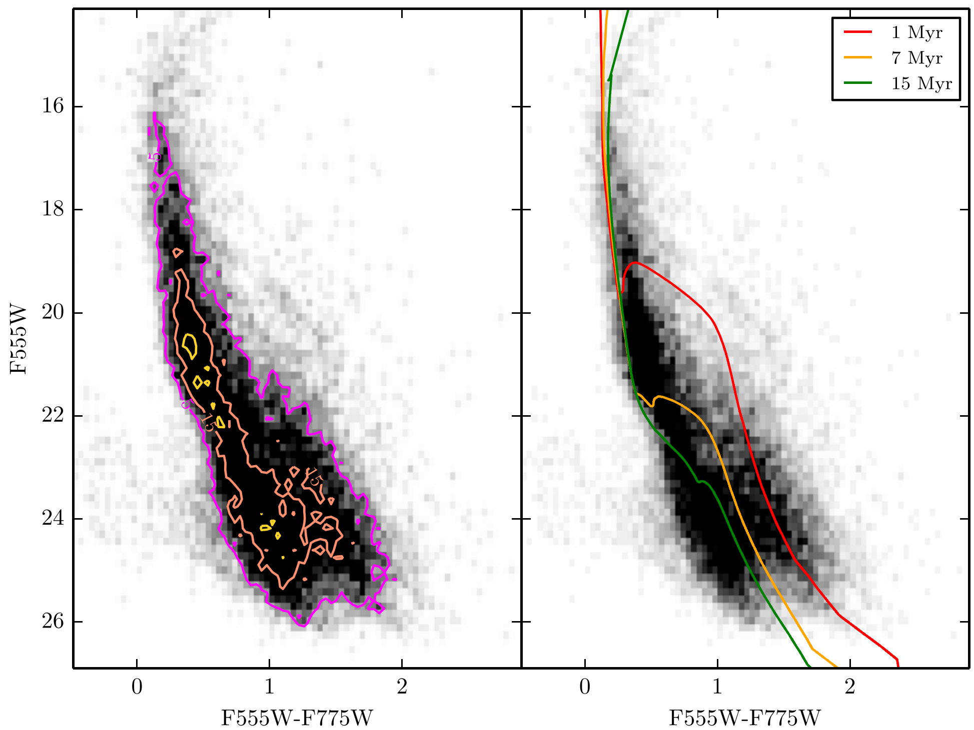

Figure 5. CMD of NGC 2070 with isodensities overlaid (left panel) and PARSEC isochrones of 1, 7, and 15 Myr overlaid (right panel). The adopted distance modulus $(m - M)_0$ is 18.5 and $E(B - V) = 0.3$.

Figures 5 and 6 in Harris & Zaritsky 1999). Other interesting features are as follows:

(1) The UMS stars (bottom-left panel in Figure 4) appear very clustered. Three major concentrations are visible: NGC 2070, the most prominent, about 40 pc wide (encircled in blue); Hodge 301 (encircled in green); and NGC 2060 (encircled in cyan). Lighter overdensities are also visible throughout the FOV. In other words, although most of the ongoing and recent (i.e., in the last 50 Myr) SF is concentrated in a few dense loci, minor recent activity is present in the entire area.

(2) Compared to the UMS distribution, the RC distribution (bottom-right panel) is, as expected, rather uniform. RC stars are a pure sample of field stars. Their age, older than 700 Myr, rules out that these objects are associated with 30 Doradus, which is, at most, a few megayears old. The small overdensities are probably contamination by intermediate-mass PMS stars or very reddened massive stars from the youngest regions. From a theoretical point of view, the intrinsic position of the RC in the CMD could be affected by factors like binaries, differences in age, and metallicity (see, e.g., Castellani et al. 2000). However, these effects are insufficient to account for the observed RC elongation (up to 1.5 mag in F555W−F775W), which is mostly due to differential reddening. The source of this reddening is the gas or dust located between the closest and farthest RC stars along the line of sight. More specifically, background RC stars suffer the highest degree of absorption, which is caused by the combination of Milky Way and 30 Doradus extinction, while foreground stars will suffer only from MW ($E(B - V) \sim 0.07$) extinction.

(3) The distributions of LMS (top-left panel) and PMS (top-right panel) stars appear mutually exclusive: the top-left corner of the FOV shows a paucity of PMS stars, while LMS stars are clearly overabundant there. The main cause for this effect is reddening. Most of the LMS stars belong to the LMC field. This is because 30 Doradus is younger than a few tens of megayears, so its MS stars are necessarily brighter than our LMS box of Figure 3 (right panel) (at ages <10 Myr the 30 Doradus low-mass stars are mainly still in the PMS, as suggested by the isochrones in Figure 3). Under these circumstances, the only way to remove LMS stars from the LMS box is the action of reddening (see also the map of Figure 8). Doing so, these reddened MS stars are likely to fill the PMS box, eventually producing the observed anticorrelation LMS/PMS stars (a similar behavior is found by Gouliermis et al. 2006 in NGC 346; see their Figure 4). In addition to this, the tendency of young PMS stars to be concentrated where the optical depth is higher exacerbates this effect. The only exceptions are the center of NGC 2070, where the LMS stars are missed because of the severe incompleteness, and Hodge 301, whose high concentration of LMS is due to its higher age (so the TOn of Hodge 301 gets into the LMS box).

Finally, the blue circle in Figure 4 is the region we have used to recover the SFH of NGC 2070. It is immediately clear from the maps that the region harbors most of the UMS stars of the entire 30 Doradus complex, as well as a remarkable concentration of PMS stars. On the other hand, the region is quite deficient in LMS stars, probably lost because of the extreme crowding conditions.

4.2. NGC 2070

In this section we discuss the broad CMD features of the stellar population of NGC 2070. Our selection includes all stars within 2000 pixels (≈20 pc) from the central R136.[12] Figure 5 shows the corresponding CMD for the F555W versus F555W −F775W filters with overlaid isodensity contours (left panel)

[12] Throughout the paper we will refer to R136 as the NGC 2070 center because it is spatially well defined.

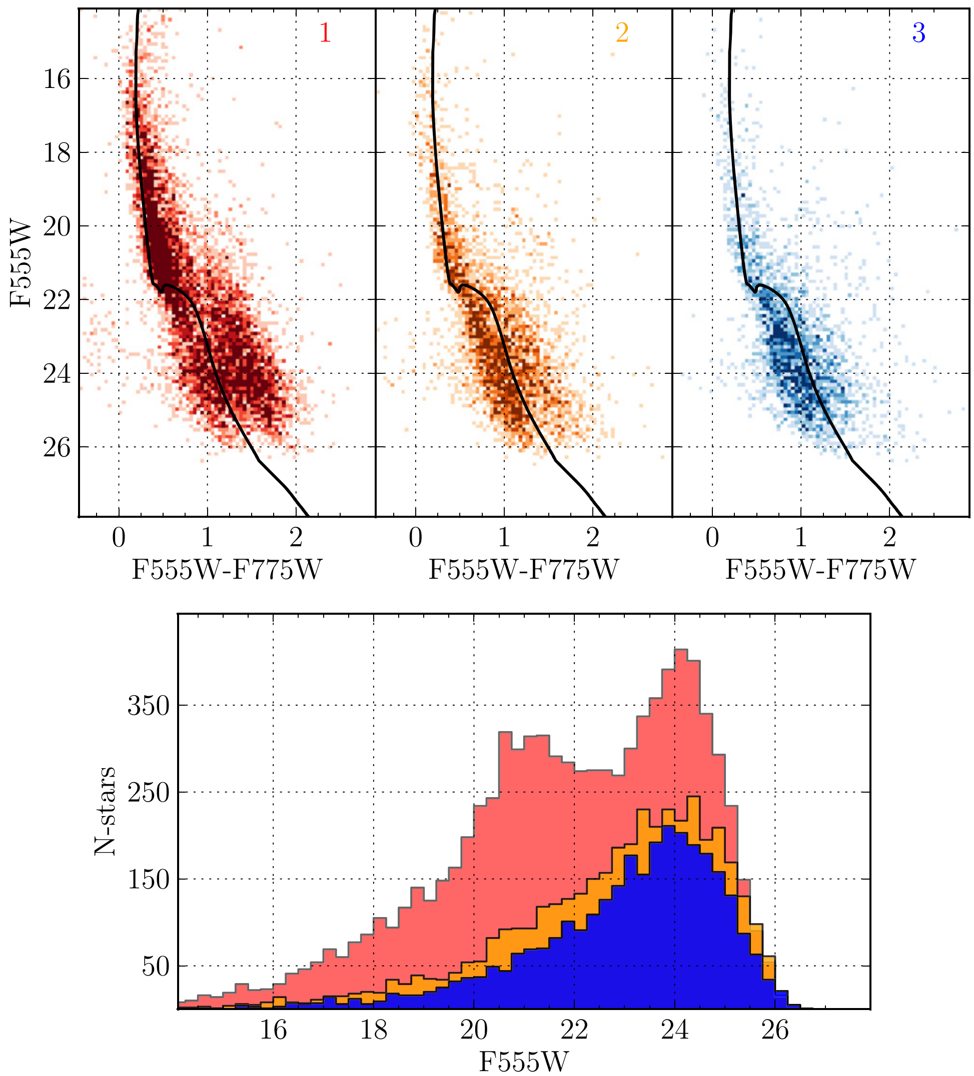

Figure 6. NGC 2070 radial distribution. Top panels: from left to right, stars from progressively more external annular regions of equal area centered on R136. A 7 Myr old isochrone is also shown to guide the eye. Lower panel: the corresponding LFs.

and PARSEC isochrones of 1, 7, and 15 Myr (right panel). The MS contours of NGC 2070 differ from those of 30 Doradus as a whole (Figure 3). The peak density is around F555W $\approx$ 21, with minor peaks down to F555W $\approx$ 22, while the 30 Doradus CMD shows a smooth profile down to F555W $\approx$ 24.

In Figure 6 we investigate the radial distribution of stars in NGC 2070. The top panels show CMDs of stars in concentric annuli of equal area (the radius of the innermost circle is about 12 pc; see Figure 7) centered on R136 (from left to right, progressively farther out from the center), and the bottom panel shows the corresponding luminosity functions (LFs). We find the following:

(1) The LF of the innermost region 1 shows two clear peaks, located at F555W $\approx$ 21 and F555W $\approx$ 24. The bright peak is well fitted by an isochrone of 7 Myr (see the figure), evidence of a young TOn. Stars brighter than this magnitude are mostly MS cluster members, whereas fainter stars are members only if they are on the PMS (by the definition of TOn, fainter members have not reached the MS yet). Indeed, a visual inspection of the CMD shows a clear color bimodality below F555W $\approx$ 21, which is likely due to field MS stars (mostly nonmembers) on the blue side, and PMS stars (members) on the red side. The dip after the bright peak is caused by the short evolutionary timescale of the PMS phase compared to the MS. After the dip, the LF rises again following the IMF, which increases at lower masses. Eventually the incompleteness wins, creating the second decline at F555W $\approx$ 24. The apparent lack of lower MS stars in region 1 is probably due to the higher crowding, which causes more severe incompleteness than in the more external annuli 2 and 3. In Section 5 we will use the synthetic CMD approach, combined with artificial star experiments, to test if these lower MS stars are compatible with LMC field contamination or hide some older TOns. To this aim, we also need to estimate the LMC contamination in a reference field (see next section).

(2) In contrast to the innermost region 1, annular regions 2 and 3 show a monotonic increase toward fainter magnitudes, with no intermediate peak before the final drop, due to incompleteness. In terms of age, the lack of obvious TOns means that regions 2 and 3 are not dominated by as young stars, as in region 1. Nonetheless, at the magnitude of the region 1 peak, region 2's LF has a mild excess of stars compared to region 3, which would point to a poorly populated TOn. As a

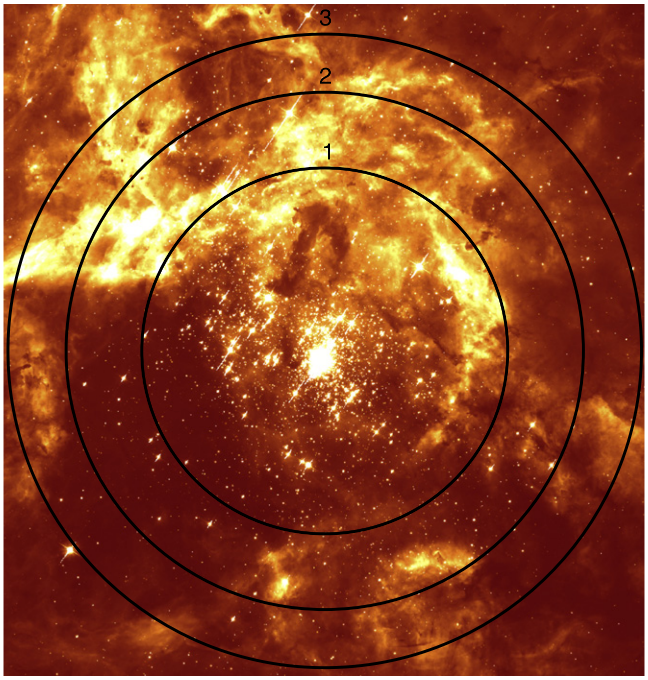

Figure 7. Concentric regions (1–2–3) of equal area overlaid on the F555W image of NGC 2070.

further proof, the region 2 CMD also shows an excess of PMS stars relative to region 3.

(3) Stars brighter than $V \sim 18$ in region 3 show a larger color spread than those in regions 1 and 2. The RC is clearly visible in regions 1 and 2 (at magnitudes 20.0−20.3 and colors 1 −1.5), while it is much more dispersed in 3. All of these suggest a differential reddening that is higher in region 3 than in regions 1 and 2.

5. RECOVERING THE SFH OF NGC 2070

The technique of recovering the SFH of spatially resolved populations from their CMDs (e.g., Tosi et al. 1991) has undergone continuous refinement and can now provide reliable SFHs for any resolved population within ≈20 Mpc (see, e.g., Tolstoy et al. 2009; Cignoni & Tosi 2010 and references therein). These advances have been achieved because of improved models of stellar evolution, which are now computed for fine grids of stellar masses and metallicities and faster multi-CPU computing facilities, which allow one to perform extensive artificial star tests on the real images and to fully explore a wide parameter space.

A widely used approach consists of populating a two-dimensional array of basic synthetic CMDs generated from stellar models. Each basic CMD is a "fuzzy" isochrone, with duration Δt, a fixed metallicity, and an assumed IMF. To compare the basic CMDs and the observational counterparts, the models are convolved with photometric errors and incompleteness as derived from artificial star tests performed on the real images. The best superposition of the basic CMDs defines the SFH and the age–metallicity relation and is the one that minimizes the residuals from the observational CMD. The approach adopted here is described in more details in the appendix.

Despite the advances in this field, the derivation of the SFH from the CMD is often affected by systematic errors that are difficult to assess. From a theoretical point of view, several stellar phases are still uncertain (thermally pulsing asymptotic giant branch, PMS, and post-MS for massive stars), while observationally differential reddening and highly variable incompleteness can be hard to treat.

Concerning NGC 2070 and the general 30 Doradus region, we face three major problems in trying to estimate the SFH: (1) there are membership errors due to field interlopers from the LMC field that mimic older populations; (2) the extreme crowding conditions exacerbate the incompleteness, shortening the reachable look-back time; and (3) the high level of differential reddening spreads and dims the CMD, blending together young PMS stars and older MS stars, which introduces further age ambiguities.

5.1. Field Contamination

To measure the SFH of NGC 2070, we need to estimate the local field contamination. A typical approach is to decontaminate the cluster by subtracting the star counts from a reference field. However, given reddening and incompleteness variations across the whole 30 Doradus, it is impossible to find another direction replicating the observational conditions of NGC 2070. A way out is to find a field that resembles as much as possible the LMC field *we would observe without* NGC 2070, which means low or negligible SF activity in the last 50 Myr, minimal differential reddening, and high completeness down to F555W $\sim$ 24. This reference LMC field could be then artificially corrected for the more severe incompleteness and photometric errors of NGC 2070. The resulting field would differ only in terms of normalization and differential reddening from the real LMC field contaminating NGC 2070. Finally, reddening and normalization of this field could be tuned together with the SFH of NGC 2070 until an adequate match of NGC 2070's CMD is found.

As a first step, we searched for low-reddening areas around 30 Doradus. A good tracer for extinction is the RC color. Figure 8 shows the spatial distribution of RC stars, color coded according to the F555W−F775W color (larger and redder symbols correspond to redder F555W−F775W). We find that, at odds with the smooth distribution of the entire RC sample (see the bottom-right panel of Figure 4), redder RC stars are very concentrated along filaments and arcs, most likely tracing gas and dust in 30 Doradus. This allows us to select extended regions, like the wide region just above NGC 2070 (see the black box in the figure), with relatively blue RC stars. Because these stars cannot all be in the foreground, these regions must be low-extinction windows in the gas and dust layers of 30 Doradus. Interestingly, the aforementioned region is also poorly populated by PMS stars (see top-right panel of Figure 4), which implies minimal SF activity in the last 50 Myr.

After a careful inspection of all regions with low extinction and PMS number, we found the best compromise in the region delineated by a black line in Figure 8. The corresponding CMD is shown in Figure 9, here overlaid on the 30 Doradus CMD (gray symbols). This sample was adopted to represent our reference field. As expected, its RC and lower MS are much tighter than the general CMD, signatures of scarce differential reddening and young SF activity, respectively. It is worth noting, however, that residual differential reddening is still present.

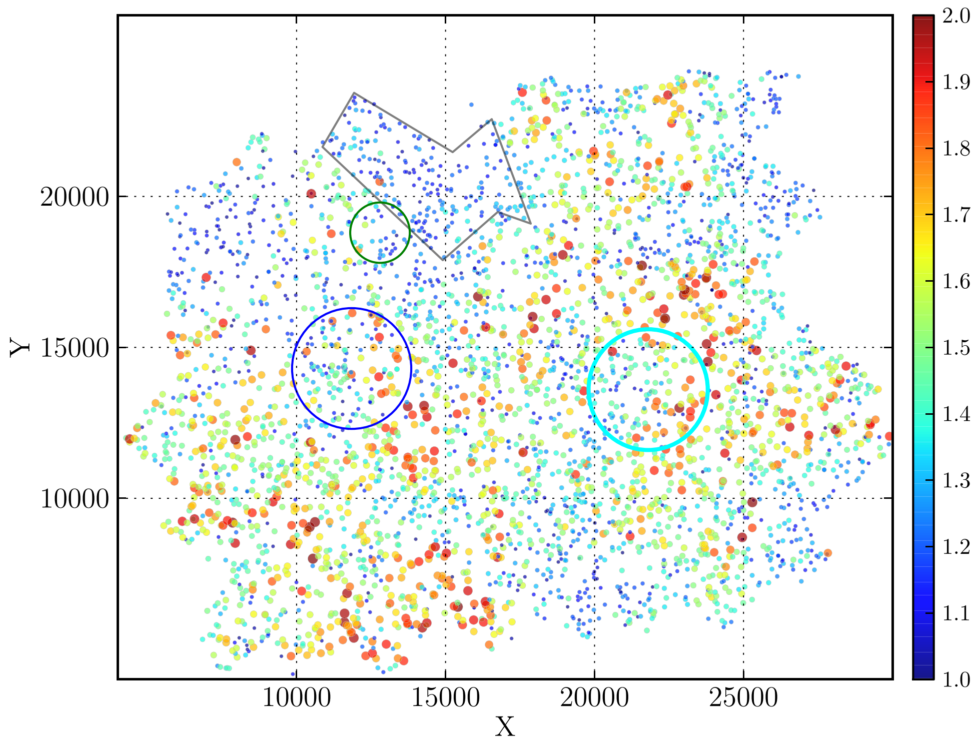

Figure 8. Spatial distribution of RC stars color coded according to their F555W−F775W color as given on the vertical bar on the right. The area delineated by a black line represents a region with low extinction (see text). Blue, green, and cyan circles highlight the regions of NGC 2070, Hodge 301, and NGC 2060, respectively.

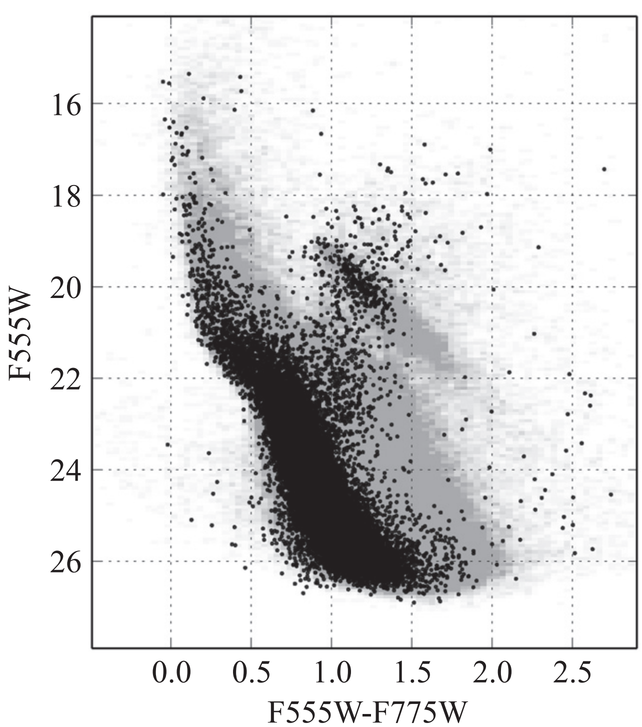

Figure 9. CMD for the reference field (black dots) overlaid on the entire 30 Doradus sample (gray dots).

5.2. Artificial-star Tests

To test the level of completeness of our photometric data and to have reliable estimates of photometric errors, we ran extensive artificial-star experiments. The experiments consist of adding "fake" sources for each of the eight passbands, modeled with the PSF used in the photometric analysis of the frames, onto the actual images. We then applied the same source-detection routines used for our science images to the fields containing the combined actual images and the fake sources. We then determined the completeness fractions, defined as the ratio of recovered artificial stars to the number of the injected ones. We considered an artificial star lost if it is not recovered or if it is recovered being 0.75 mag brighter than its input magnitude. In fact, this means that it has fallen either on a real star brighter than the artificial star or one of the same brightness. Thus, we are not recovering or measuring the artificial star but a real one instead.

To preserve the crowding conditions of the data, fake stars were arranged in a spatial grid such that the separation of the centers in each star pair was larger than two PSF radii. We found that a separation of 20 pixels guarantees that the probability of recovering a fake star is the same as it would be if we added only one fake star. The experiment is then repeated using a series of slightly shifted grids.

As an example of our fake stars procedure, the top panel of Figure 10 shows the impressive 50% completeness map in the F555W band for a region 2000 pixels ($\approx$20 pc) away from the center of NGC 2070 (5 million fake stars). The bottom panel shows the corresponding real image. The most striking feature is the remarkable completeness variation, up to 8 mag, in different locations within the region. Regions like the broad area around $X = 10750$, $Y = 13500$ are photometrically complete at the 50% level down to $V \approx 26$, whereas more crowded subregions, like the central area, are 50% complete only for $V < 20$. Such variations are determined by the interplay of four major effects: photon scattering off dust in 30 Doradus, continuum/line nebular emission, pixel saturation, and stellar crowding. Dust scattering and gas emission raise the

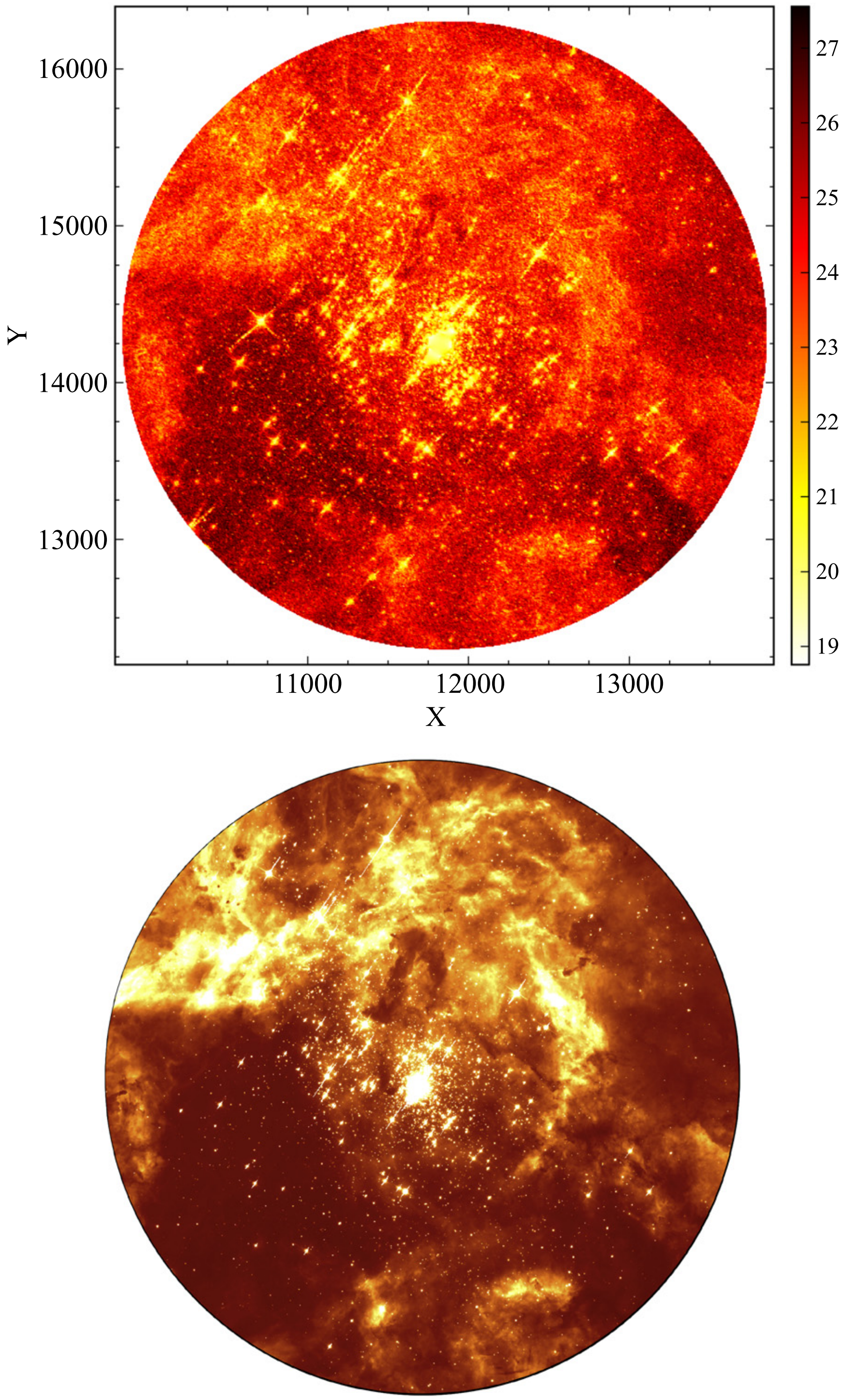

Figure 10. Top panel: completeness map for NGC 2070 color coded according to the F555W magnitude where the sample is 50% complete (which means that 50% of the injected artificial stars are recovered). The highly incomplete central region is R136. Bottom panel: the real image of the region in the filter F555W.

background flux and, in turn, make it more difficult to resolve stars. The net result is visible in the diffuse "nebulous" areas of the completeness map (see Figure 10). More localized than the dust and gas effects, pixel saturation produces the visible "streaks" (charge-bleeding along the rows of the CCD) extending off of many bright stars. Finally, the extreme crowding conditions near R136 are responsible for the central completeness "hole" (where most of the injected fake stars are lost).

5.3. Reddening and Data-model Comparison

We are not assuming any a priori reddening distribution. In principle we do not know where populations of different age are located *inside* NGC 2070, so reddening is an unknown function of age. Naively speaking, young massive stars may have carved the gas with their ionizing flux, hence lowering the extinction. On the other hand, high levels of SF could be sustained only where the gas density is higher, which would lead to the opposite situation. Besides, normalization and

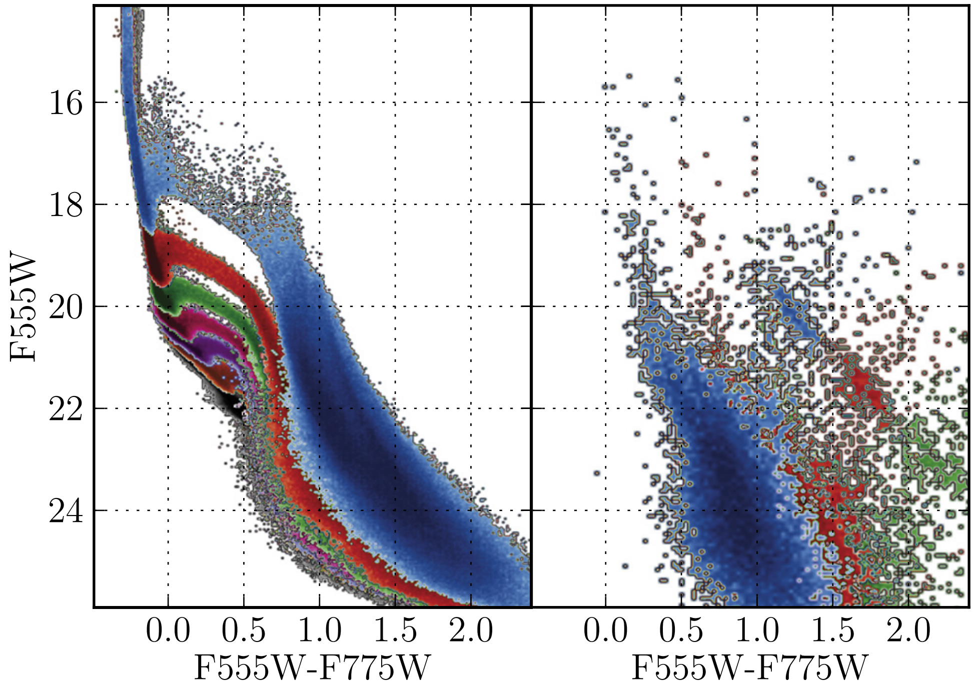

Figure 11. Left panel: example of "basic" synthetic CMDs generated with distance modulus $(m - M)\,0 = 18.5$ and $E(B - V)$ in the range 0–0.05 mag, color coded with age: blue, red, green, purple, violet, orange, and black stars have ages in the range 0–1 Myr, 2–3 Myr, 4–5 Myr, 6–7 Myr, 8–9 Myr, 10–12 Myr, 14–16 Myr, respectively. Right panel: example of "basic" field CMDs color coded with reddening: blue, red, and green stars are field stars artificially reddened with $E(B - V)$ in the range 0–0.05 mag, 0.35–0.40 mag, and 0.70–0.75 mag, respectively.

reddening of the reference field are also free parameters. Furthermore, PMS stars may appear reddened due to their local circumstellar material.

When dealing with such a large parameter space (age, reddening, and field contamination) there is uncertainty on whether the best solution is local or global. To cope with this, we combined a genetic algorithm with a local search procedure called a hybrid genetic algorithm (HGA; see Appendix A.1 for details), which is more effective in avoiding local trapping than local search alone. In our approach, the first step is to store a library of "basic" synthetic CMDs, where each CMD is a Monte Carlo synthetic population generated with a step-wise SF and reddening distribution.

When the CMDs are generated, other population parameters like metallicity, distance modulus $(m - M)_0$, slope of the IMF, and binary fraction q are kept fixed at 0.008 (e.g., Luck et al. 1998), 18.5 (e.g., Panagia et al. 1991; Schaefer 2008; Pietrzyński et al. 2013), Kroupa (2001), and 30%,[13] respectively. The explored ages range from now up to 50 Myr ago. Since older isochrones tend to be more tightly packed in the CMD than younger isochrones, the duration of each age step increases with age from 1 Myr (at the present time) to 20 Myr (50 Myr ago). The reddening is allowed to vary between 0 and 1 mag with a step of 0.05 mag, while the extinction coefficients R_λ are taken from De Marchi & Panagia (2014), who derived them using RC stars in a region ~2.7 arcmin × 2.7 arcmin enclosing NGC 2070.

All "basic" synthetic CMDs (see left panel of Figure 11) are then degraded using the photometric errors and incompleteness as derived from the artificial star tests discussed in the previous section. Once this basis is generated, any complex synthetic CMD can be constructed as a linear combination of the "basic" synthetic CMDs. In order to take into account field contamination, the CMD of the reference field (see Section 5.1) is artificially reddened with steps of 0.05 mag between $E(B - V) = 0$ and $E(B - V) = 1$ to produce a complete basis of field CMDs. Likewise, any kind of contamination can be simulated by linearly combining these "basic" field CMDs (see right panel of Figure 11). The only difference is that the "basic" field CMDs are corrected for the *difference* in photometric errors and incompleteness as estimated in the field itself and in the NGC 2070 region, while the "basic" synthetic CMDs are only corrected for the latter. However, since in the reference field completeness and photometric errors at F555W ~ 24 are 100% and $1/20$ of the error in subregion A1, the first correction is almost negligible. The combination of "basic" CMDs (both synthetic and field) that minimizes the residuals from the observational CMD (in terms of Poissonian likelihood) is searched with the HGA code. The best coefficients tell us the most likely: (1) SF rate as a function of time (i.e., the SFH); (2) total reddening (foreground + internal) as a function of time; and (3) field contamination (reddening and normalization).

Which part of the CMD is used? Not all of the CMD is used to recover the SFH. Our analysis is limited on the bright end by the saturation magnitude and on the faint end by the 50% completeness magnitude level. Nonetheless, even with these conservative selections, the large variations of completeness with magnitude in some regions (see upper plot in Figure 10) force us to derive the SFH in subregions within which the completeness is reasonably uniform. In fact, our artificial stars are uniformly distributed across the region, whereas real stars are concentrated in clumps and filaments, structures covering a minor fraction of the total area. As a consequence, most of the stars will suffer a real incompleteness that is worse than the average measured with artificial stars. The division in "isocomplete" subregions mitigates this bias. Figure 12 shows

[13] Primary and secondary stars are both picked from the same IMF.

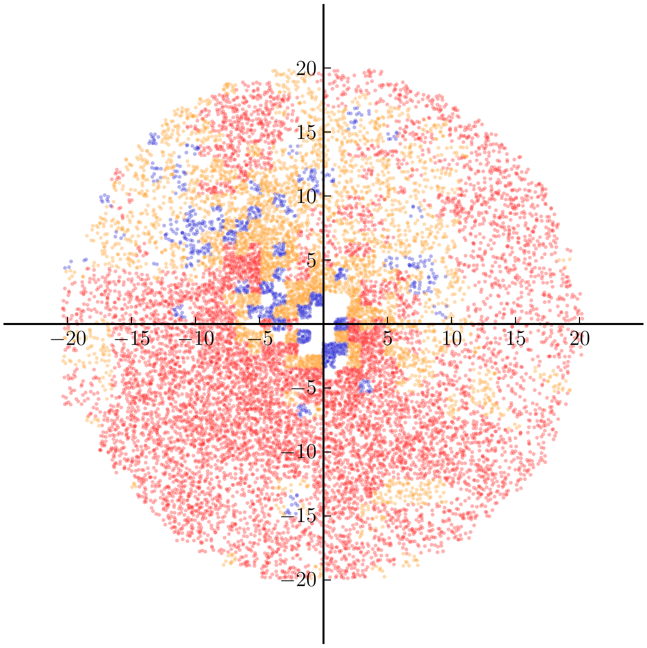

Figure 12. Subregions of NGC 2070 where the average completeness is 50% for F555W > 24 (A1; red dots), 23 < F555W < 24 (A2; orange dots), and 22 < F555W < 23 (A3; blue dots).

our selection: subregions of NGC 2070 where the completeness in F555W is 50% for F555W > 24 (A1), 23 < F555W < 24 (A2), and 22 < F555W < 23 (A3) are indicated in red, orange, and blue, respectively. The stars found in both the F555W and F775W filters inside these subregions are used to recover the optical SFHs. Overall, our subregions trace the stellar density, from the lowest (A1) to the highest (A3).

This analysis leaves out the very center of NGC 2070, a ≈3 pc region mostly represented by the SSC R136, and part of the so-called "northeast clump" (the three little holes in the top-left quadrant of the map in Figure 12), an agglomerate of stars a few parsecs away from R136 (see e.g., Sabbi et al. 2012). In these two regions, stellar crowding is so severe that most of the intermediate- and low-mass stars are lost, so little, if any, information is available from TOns.

To further validate the SFH, we independently analized the NIR data. To do this we used all stars detected in both the F110W and F160W images inside each subregion (defined using the F555W data). In this case, however, the faint limiting magnitude was anchored to the 50% completeness level in F110W.

6. RESULTS

6.1. SFHs

Figures 13 and 14 show the recovered SF rate (in $M_\odot$ yr^{-1} pc^{-2}; top panel), reddening (middle panel), and stellar mass (bottom panel) as a function of time for subregions A1 and A2, respectively, as predicted using the optical (green curve) and NIR (red curve) CMDs. In principle, our code provides the full distribution of reddening as a function of age, but to ease the visualization we only provide the mass-weighted[14] average reddening as a function of age. The shaded bands indicate one (darker) and two (lighter) standard deviations. Such uncertainties are the quadrature sum of a statistical error (obtained by bootstrapping the data and rederiving the solutions) and systematic error (obtained by rederiving the solutions with different age binnings and CMD binning scheme).

Despite the different spatial resolution and reddening sensitivity, the optical and NIR predictions are in good agreement. Both results predict that mild SF activity started throughout the whole NGC 2070 region ≈20 Myr ago, and that about 7–8 Myr ago the birth rate accelerated. Interestingly, the activity in the last 1 Myr has been relatively quiet compared to the average in the last 5 Myr. However, we note that 1 Myr is also the characteristic time required by stellar models to forget arbitrary initial conditions, conditions that could be over-simplified[15] (a fully convective object starting its contraction along the Hayashi line; see the discussion in Baraffe et al. 2002). For this reason, the recovered activity in the last 1 Myr (the hatched bin in Figures 13, 14, 16) could be an unphysical artifact of the models (see also the discussion in the next section).

Concerning the activity that commenced 20 Myr ago, it is important to note that our SFHs have been obtained by taking into account field contamination, so, unless we have been very unlucky in our field selection[16], it is reasonable to assume that this activity is a local extra over the LMC field. Nonetheless, whatever the origin, its significance is low (zero activity is still within 1σ error bars).

Focusing on the specific subregions, the SFH of subregion A1 shows a mild bimodality, with a minor peak around 5–7 Myr ago and a major peak 1–4 Myr ago (1–3 Myr ago in the optical SFH, 2–4 Myr ago in the NIR one). The measured reddening distribution anticorrelates with SF: the average $E(B-V)$ is ≈0.6 for stars with ages older than 7 Myr, when the SF activity was lower, and ≈0.4 for stars of younger ages, when the SF was stronger. Optical and NIR reddening derivations agree within errors, both in confirming the presence of notable differential reddening. The large oscillations of the NIR solution are mostly due to the low sensitivity to reddening in these filters. Figure 15 shows an example of the full reddening solution (number of considered stars versus $E(B-V)$) for subregion A1 in three age bins (2, 6, and 20 Myr). As can be seen, the full distributions are asymmetric with a long tail at high reddening.

The SF in subregion A2 (Figure 14) is about two times higher than in subregion A1. The most important feature in the A2 SF is a pronounced peak in both optical and NIR solutions 1–3 Myr ago. Like in subregion A1, the reddening of subregion A2 is anticorrelated with the SF activity. The average reddening values are also very similar.

Figure 16 shows the SFH in the subregion A3 over the last 25 Myr (the crowding conditions prevented investigation of earlier activity). The peak activity in both the optical and NIR solution is more than two times higher than in A2, and, at odds with other subregions, it is clearly located between 1 and 2 Myr ago (more pronounced in the NIR solution).

Figure 17 compares the SF in the three subregions for the optical (top panel) and the NIR (bottom panel) case. The most striking feature is an overall rejuvenation of the main SF peak

[14] Weighting with the predicted mass allows us to take into account that high reddening stars tend to be undersampled because of the incompleteness.

[15] Realistic models for ages younger than 1 Myr should depend on the outcome of the prior protostellar collapse and accretion phase.

[16] Normalization and reddening of field stars are allowed to vary, whereas the ratio between *young and old field stars* depends on the chosen field.

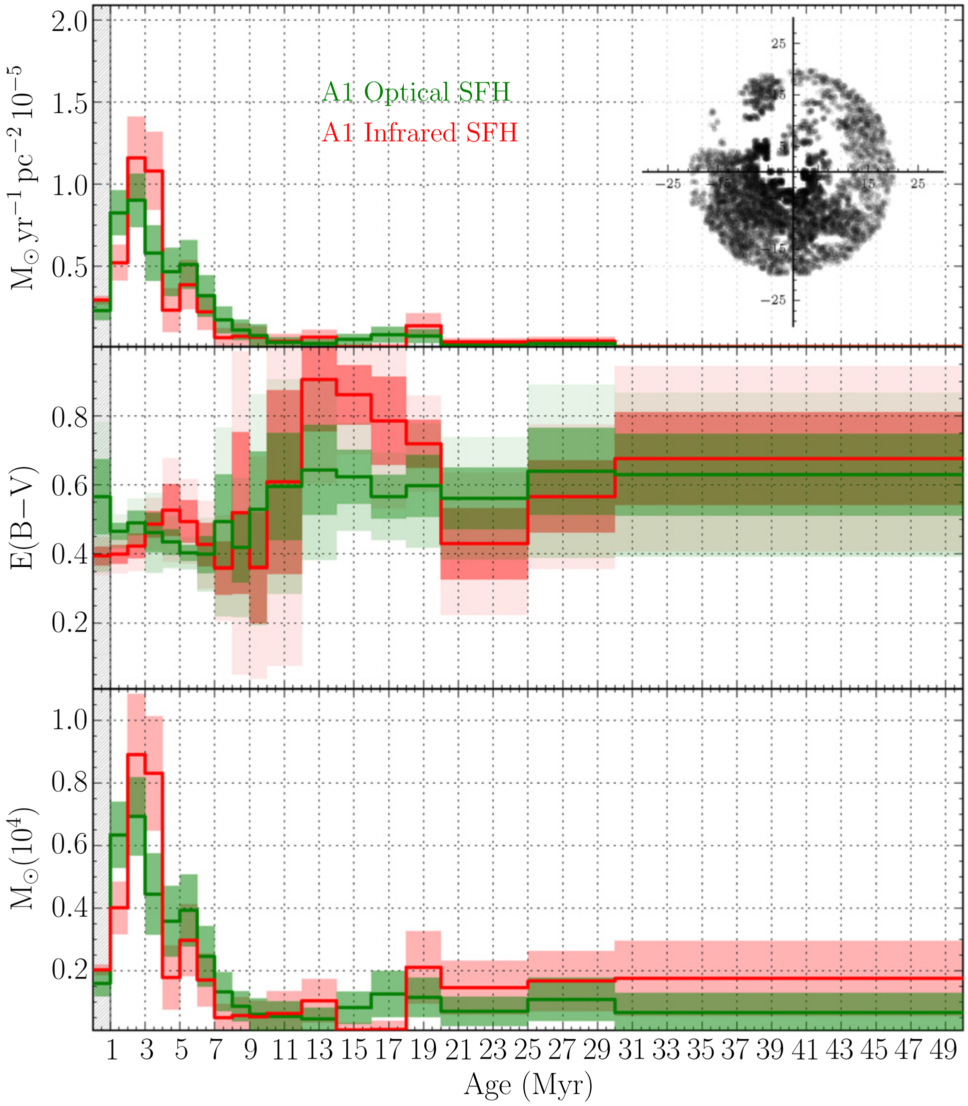

Figure 13. Recovered SFH (top panel), reddening distribution (middle panel), and mass distribution (bottom panel) for the subregion A1. The optical and NIR solutions are plotted in green and red colors, respectively. The bin showing the SF rate in the 0–1 Myr range is marked in light gray to indicate that systematic uncertainties may be comparable to or are greater than the formal errors (see text). The inset panel shows the distribution of stars in subregion A1.

from the most peripheral subregion A1 to the central A3. This effect is mildly significant in the optical, while it is strong in the NIR, probably due to the effectiveness with which the latter can penetrate dust. On the other hand, the superior resolution of the optical CMDs allows us to constrain much better the commencement of the major period of activity, about 7 Myr ago.

Finally, our analysis does not involve the central region of NGC 2070 (R136), where the activity is presumably much higher, and part of the northeast clump. A rough estimate of the total SF in the missing regions can be made by rescaling the SFH of region A3 to match the number of stars in the magnitude range F555W 16–18, where the sample is fairly complete even in R136. In this magnitude range, the missing regions (hereinafter referred to as "R136" because R136 is by far the dominant component) contain two times the stars of subregion A3, but concentrated in an area four times smaller. This leads to a scaled peak rate of the order of $2.8\times10^{-4}\,M_\odot\,yr^{-1}\,pc^{-2}$ and a total mass of $2.2\times10^{4}\,M_\odot$ (integrated over the last 7 Myr), in excellent agreement with the estimate of Hunter et al. (1995). Adding this mass estimate to the mass of subregions A1, A2, and A3 ($2.9\times10^4\,M_\odot$, $2.5\times10^4\,M_\odot$, and $1.1\times10^4\,M_\odot$, respectively, integrated over the last 7 Myr), we get a total mass for NGC 2070 of $8.7\times10^4\,M_\odot$.[17] This value is compatible with the results of Selman et al. (1999), who found $5.5\times10^4\,M_\odot$ within 14 pc from R136 (using a Salpeter IMF down to $0.5\,M_\odot$), Andersen et al. 2009, who found $2.7\times10^5\,M_\odot$ (using a Salpeter IMF down to $0.1\,M_\odot$), and Bosch et al. (2001), who found $10^5\,M_\odot$ using dynamical considerations.

In order to have a global picture of the SFH in NGC 2070, we summed up the individual SF rates of each subregion. The global rate per pc^2 (green for the optical, red for the NIR) is shown in Figure 18, with (dashed line) and without (solid line) the extrapolated contribution of R136. The global peak is clearly between 1 and 3 Myr ago (somewhat younger if R136 is included).

[17] We stress that this result has been obtained with a Kroupa (2001) IMF. Changing from a Kroupa to a Salpeter IMF below $0.5\,M_\odot$ increases the total by a factor of 1.6.

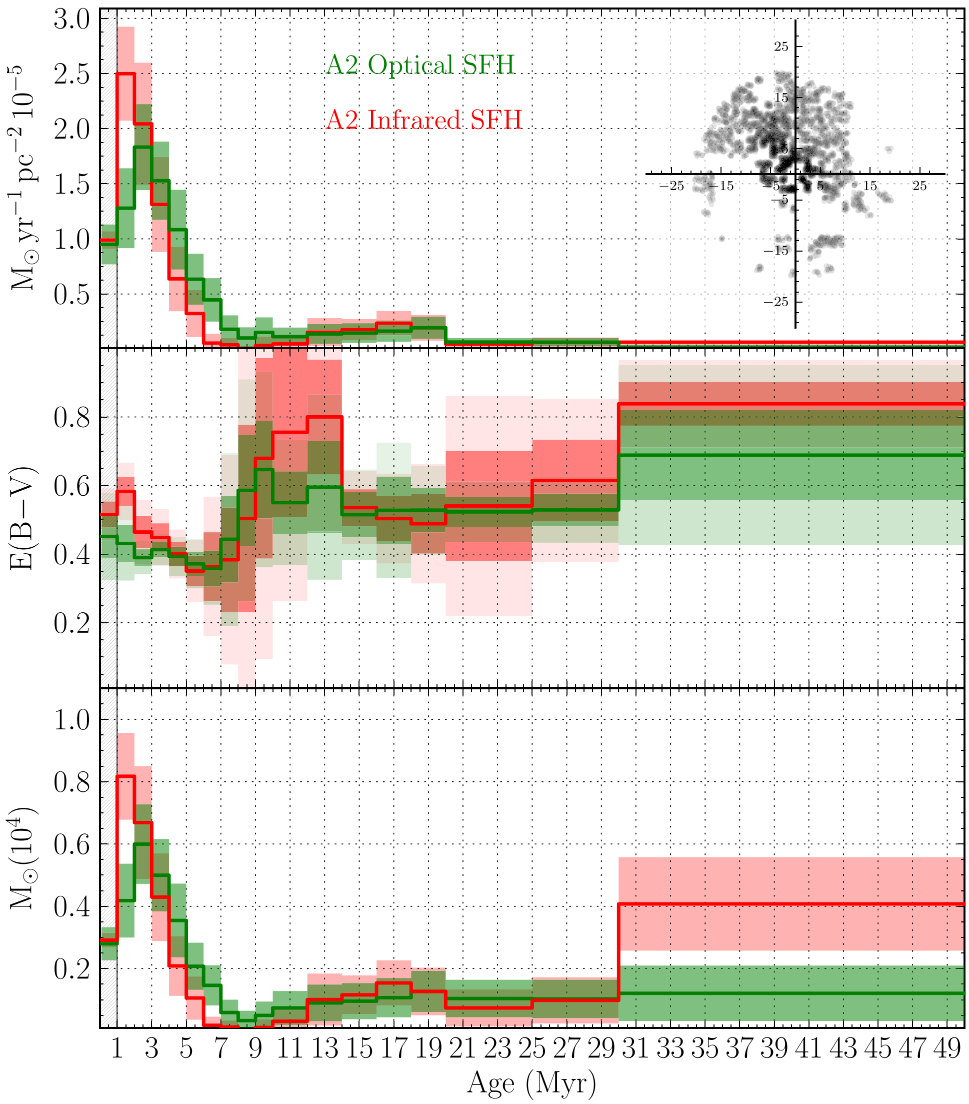

Figure 14. Same as Figure 13 but for the subregion A2.

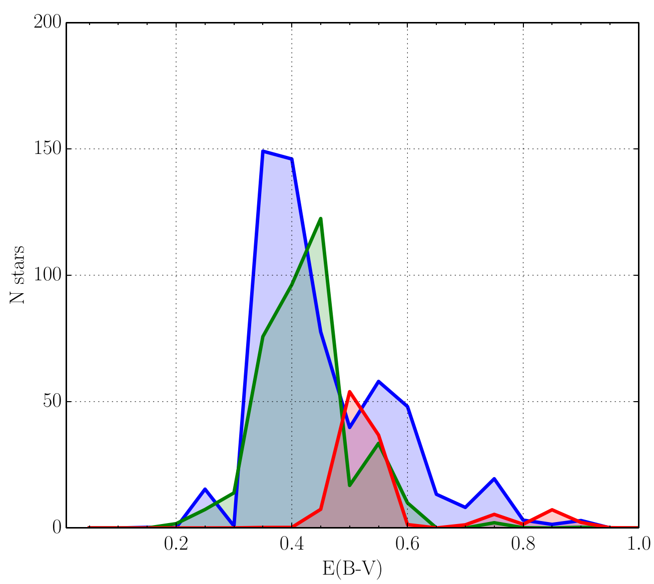

Figure 15. Predicted number of stars in subregion A1 as a function of reddening $E(B-V)$ for three age bins, 2 Myr (blue), 6 Myr (green), and 20 Myr (red).

6.2. Fit Quality

Figure 19 compares the observed optical CMDs (top panels) in the three subregions (from left to right, A1–A2–A3) to synthetic CMDs (middle panels) generated from our best solutions. The bottom panels show the corresponding LFs. The red dashed line corresponds to the faintest limit used to fit the data. Figure 20 shows the same analysis for the NIR CMDs.

Simulations for subregions A1 and A2 show a good agreement with both the optical and NIR CMDs. Within the portion of the CMDs used to fit the data (see red dashed lines), observational and model LFs show deviations that are compatible with the errors (computed as the square root of the observational count rates). This suggests that a Kroupa IMF, which is very similar to a Salpeter IMF above $0.5M_\odot$, is consistent with the data. At fainter magnitudes, our simulations systematically underestimate the observational star counts (more in the optical than in the NIR). This effect is minor in subregion A1, but becomes significant in subregion A2. One possible explanation for this mismatch is the 0.75 mag selection threshold that we used to reject artificial stars that are actually blended with real stars. Relaxing this

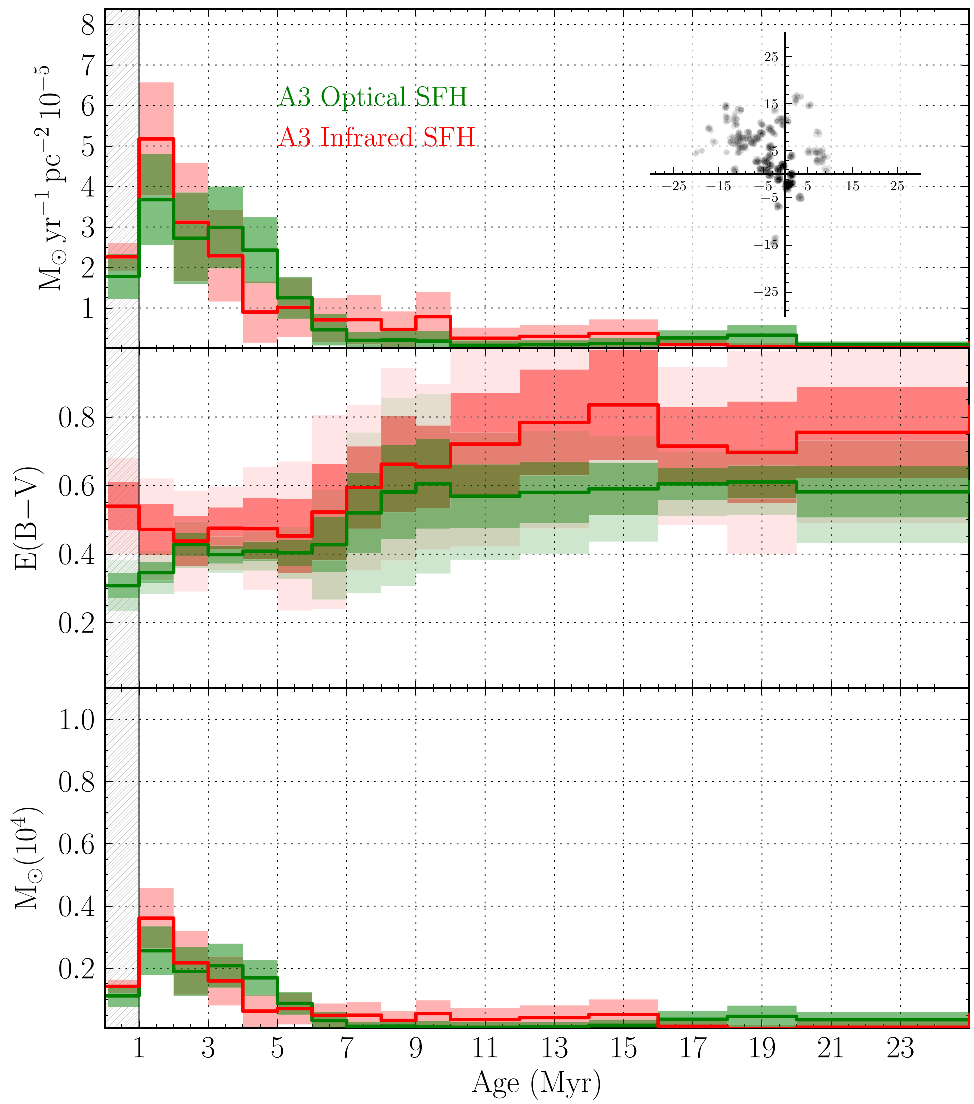

Figure 16. Same as Figure 13 but for subregion A3.

condition alleviates the issue, but also increases the scatter in the synthetic CMDs more than what we see in the data. However, the impact of this effect should be minor in the magnitude range used for fitting.

The simulation for subregion A3 is in less good agreement with the observations. As is visible from the LFs (see the bottom-right panel of Figure 19), the observed star counts systematically outnumber synthetic counts even at bright magnitudes (F555Ws < 19 and F110Ws < 18). Such a discrepancy could be mitigated using a flatter IMF above $\sim$10 $M_\odot$ instead of the assumed Kroupa. Indeed, this is what is found in other dense and young clusters like, for example, Quintuplet (Hußmann et al. 2012) and Arches (Espinoza et al. 2009). However, it is also conceivable that the transition from PMS to MS for intermediate or massive stars is not well reproduced by models. Indeed, the major discrepancy is around F555W $\sim$ 18 (F110W $\sim$ 17), which corresponds to TOn ages younger than 1 Myr. If the PMS evolutionary time for these objects is overestimated (so more PMS stars were predicted than observed) or the PMS birth-line (the region in the CMD where stars are still embedded in their gas cocoons and, therefore, still invisible in optical bands) is closer to the MS than predicted, any attempt to simultaneously fit PMS and MS star counts will end up with a bias. From this point of view, the deficiency of MS stars could suggest that the SF rate for stars younger than 1 Myr might be underestimated.

Finally, the number and colors of RC stars are well reproduced. This indicates that field contamination and reddening are correctly modeled.

6.3. Solution Robustness

To test the robustness of the solution against variations in the assumed IMF, binary prescription (fraction and mass ratio), and distance, we rederived the SFH of subregion A1 using alternative values as an example. In Figure 21 we compare the results (orange-shaded histograms) with the standard solution (green-shaded histogram). The top-left panel shows the SFH obtained using a shorter distance modulus, $(m-M)_0 = 18.4$, as suggested by some Cepheids studies (e.g., Macri et al. 2006). The top-right panel shows the SFH obtained with a binary fraction of 60% (e.g., Sana et al. 2013) and mass ratio randomly drawn from a constant distribution between 0.5 and 1. The bottom-left and bottom-right panels show the SFH

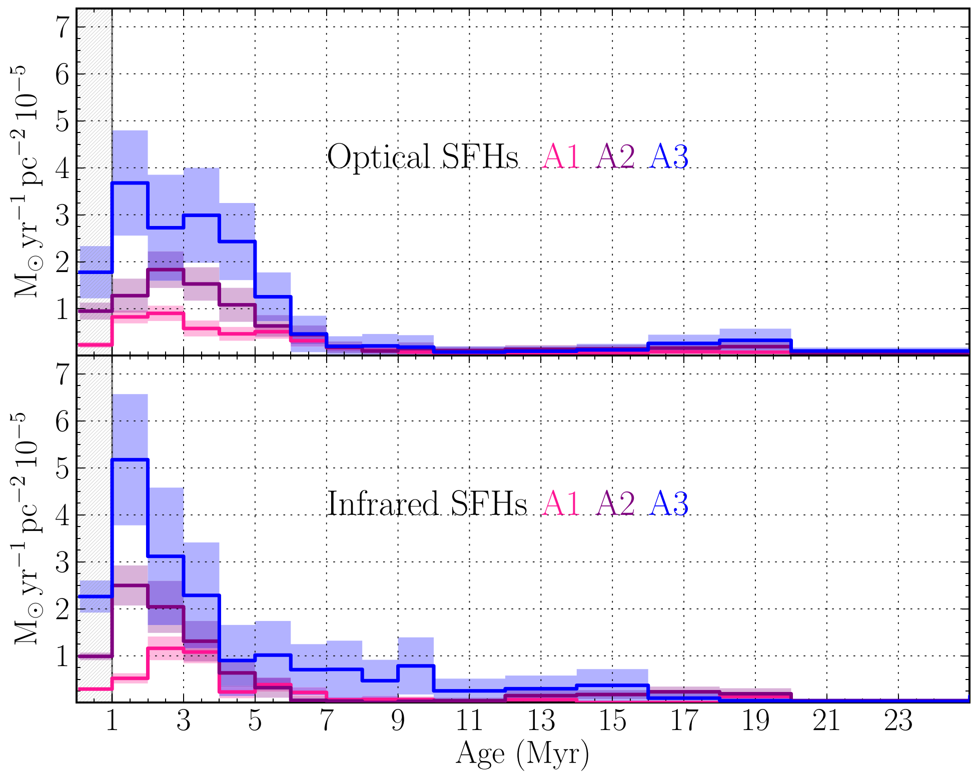

Figure 17. Optical (top panel) and NIR (bottom panel) SFHs for subregions A1 (pink), A2 (purple), and A3 (blue).

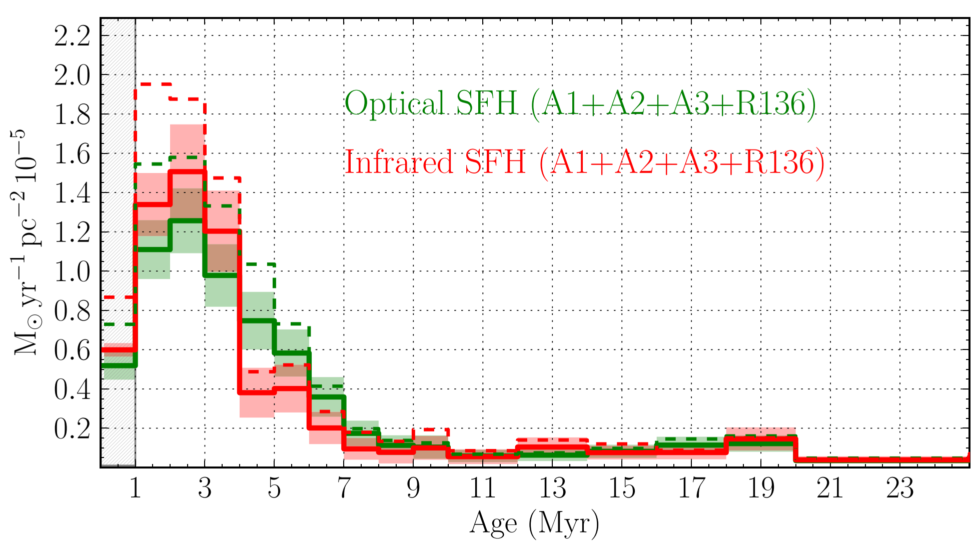

Figure 18. Solid line: total optical (green) and NIR (red) SFH of NGC 2070 (sum of A1, A2, and A3 SFHs). Dashed line: total SFH including the contribution of R136 (see text).

obtained using an IMF exponent s, above $1\,M_\odot$, of 1.9 and 2.7, respectively.

Overall, all recovered solutions are qualitatively and quantitatively (within 2σ) consistent, suggesting that our findings are robust. In particular, the onset of the major activity 7 Myr ago is unchanged. Relatively larger differences are found for IMF changes. The predicted rate for $s = 1.9$ is significantly stronger than the $s = 2.3$ case for ages > 20 Myr, while for $s = 2.7$ it is stronger for ages <5 Myr. These differences are principally due to the SF rate–IMF degeneracy. The lack of stars of lower mass (caused by the flatter IMF) is compensated for with a higher early SF rate, whereas the lack of intermediate and massive stars (caused by the steeper IMF) is compensated for with a higher recent activity.

We also found that the synthetic CMDs corresponding to the $s = 1.9$ and $s = 2.7$ solutions systematically underestimate and overestimate, respectively, the star counts for F555W < 20 (the reverse for F555W > 23). On the other hand, changing the binary fraction and mass ratio does not affect either the SFH or the fit quality.

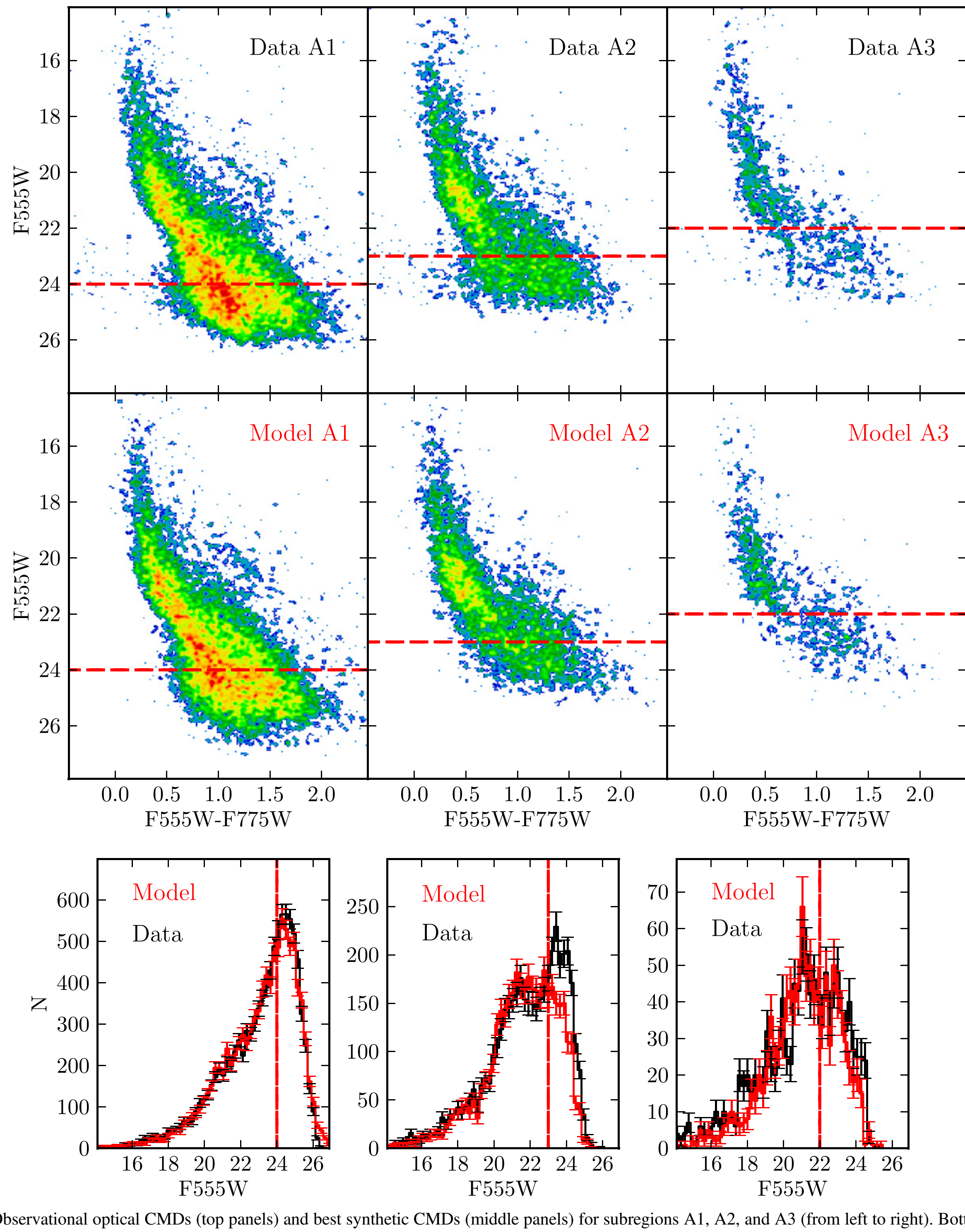

Figure 19. Observational optical CMDs (top panels) and best synthetic CMDs (middle panels) for subregions A1, A2, and A3 (from left to right). Bottom panel: data versus model LFs. The dashed line indicates the magnitude limit used to recover the SFH.

7. COMPARISON WITH PREVIOUS STUDIES

7.1. SFH

Selman et al. (1999) recovered the SFH of NGC 2070 using a Bayesian approach applied to the *UBV* photometry down to $V = 19.2$, corresponding to stars more massive than $20\,M_{\odot}$. The SFH was found to be dominated by three episodes, namely a young peak at $0 < t < 1.5$ Myr, an intermediate-age peak at $1.5 < t < 3.5$ Myr, and an old peak $4 < t < 6$ Myr ago. These three bursts appear to be spatially disjointed, with the youngest stars concentrated toward the center, and the intermediate-age stars appear to be spherically distributed over a 6 pc radius, slightly off center. The observations are consistent with an SF that propagated inward.

Andersen et al. (2009) obtained *HST*/NICMOS F160W band images of the central 14 pc $\times$ 14.25 pc around R136 and combined them with archival WFPC2 F555W and F814W observations (Hunter et al. 1995, 1996b). By fitting the F160W versus F555W$-$F160W CMD with stellar models above $7\,M_{\odot}$ (Marigo et al. 2008) and stellar models below $7\,M_{\odot}$ (Siess

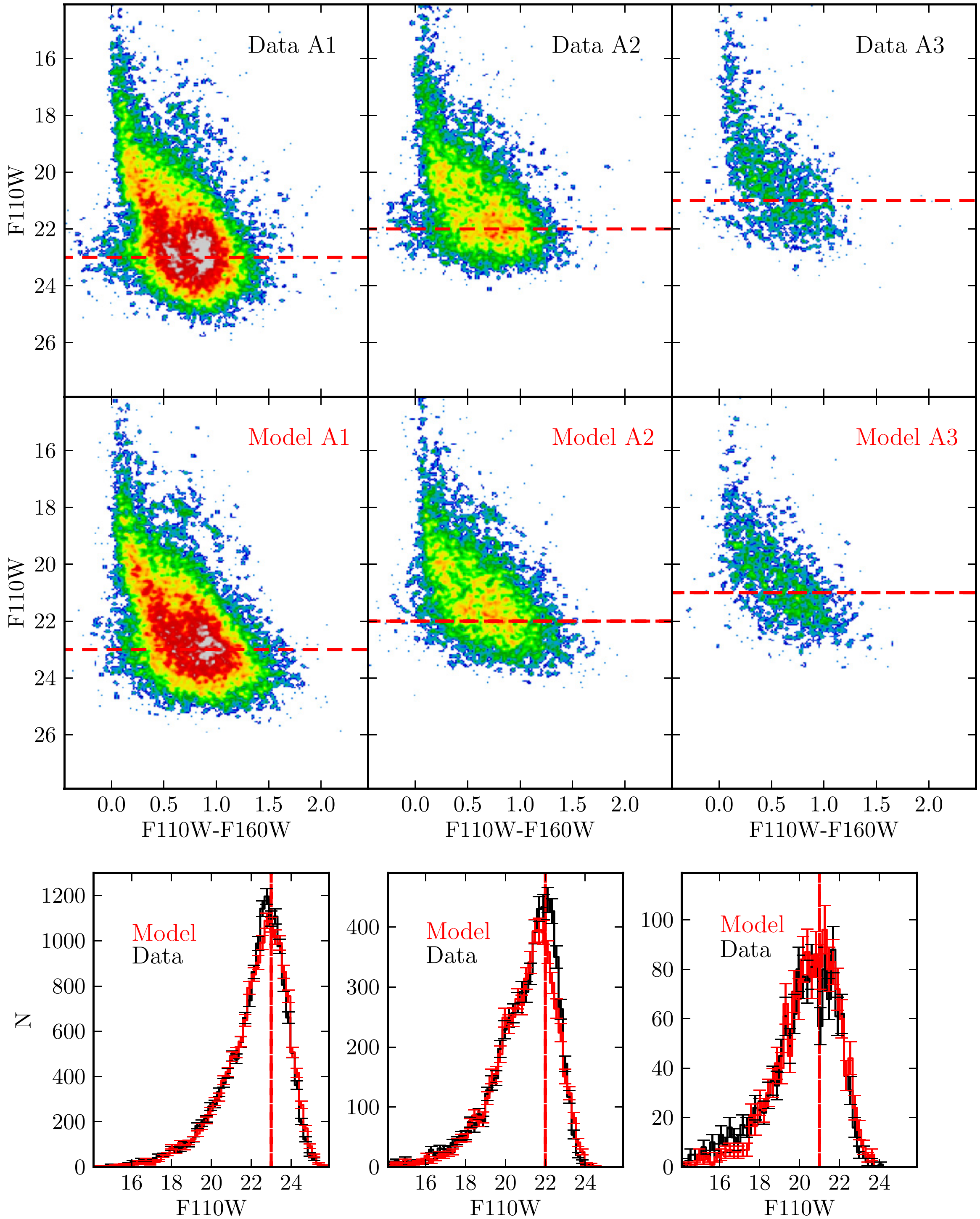

Figure 20. Same as Figure 19 but for NIR. The dashed line indicates the magnitude limit used to recover the SFH.

et al. 2000), they constrained the age of the low-mass population to be 2–4 Myr old.

Brandl et al. (1996) derived the age distribution for a region of 13×13 arcsec^2, at a distance of 4 arcsec from R136, using a synergy of NIR photometry with adaptive optics and *HST* photometry. Their investigation was limited to stars more massive than 12 $M_{\odot}$. The resulting age distribution (see their Figure 13) grows from 7 Myr ago up to the present time, with three visible bursts at 5–6 Myr, 3–4 Myr, and 1 Myr ago. Moreover, they did not find red giants and red supergiants in their FOV, concluding that the age of R136 must be less than 5 Myr.

According to Walborn & Blades (1997) the central region can be divided into a core, R136, 2–3 Myr old, a peripheral triggered population <1 Myr old, and a group of late-O and early-B stars 4–5 Myr old.

Using deep *HST* observations (including Hα) for a region enclosing NGC 2070, De Marchi et al. (2011) inferred that a significant fraction (∼35%) of the PMS stars were formed prior to 12 Myr ago, while a similar fraction is younger than 4 Myr.

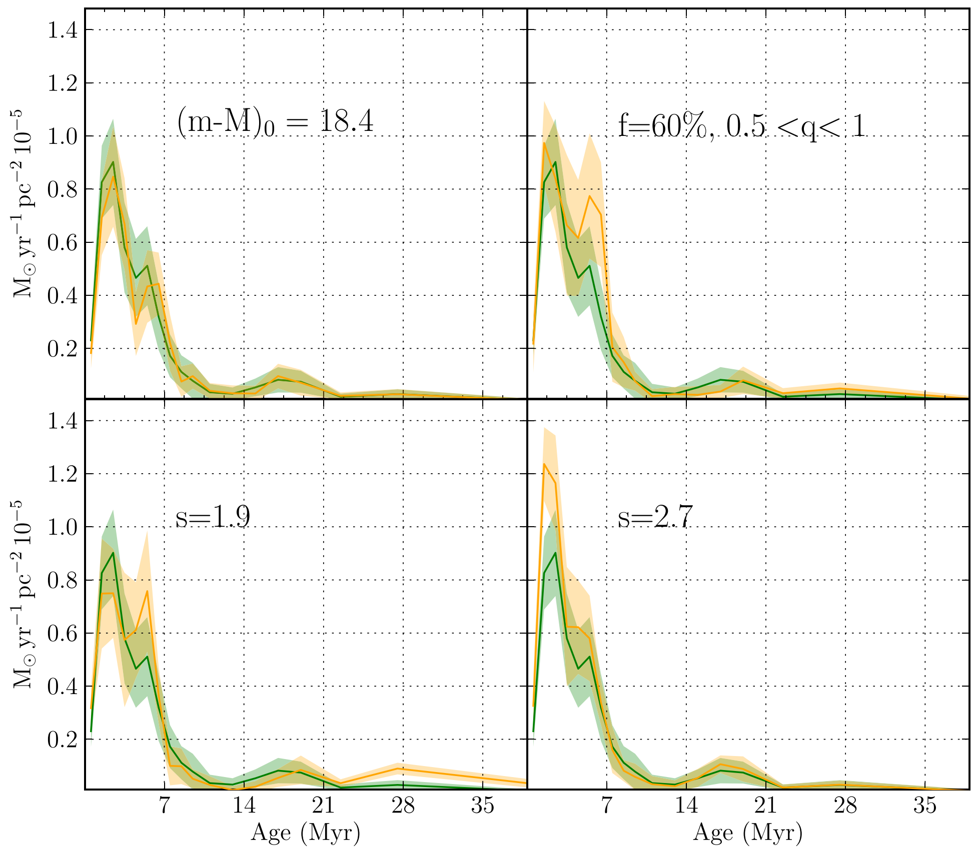

Figure 21. Sensitivity test for the SFH in subregion A1. Solutions for different assumptions for the IMF, binary population, and distance (orange-shaded histograms) are overlaid on the standard solution (green-shaded histogram). The top-left and top-right panels show the result of changing the distance and binary fraction from 18.5 and 30% (primary and secondary masses randomly paired from the same IMF) to 18.4 and 60% (mass ratio randomly drawn from a constant distribution between 0.5 and 1), respectively. The bottom-left and bottom-right panels show the result of changing the IMF exponent above 1 $M_\odot$ from 2.3 to 1.9 and 2.7, respectively.

In terms of SF, they found that 1 Myr ago the region was about 30 times more active than 16 Myr ago.

Using isochrone fitting, Sabbi et al. (2012) found that the majority of the stars in the "northeast clump" have ages between 2 and 5 Myr ago, while stars in R136 are at most 2 Myr old.

Except for De Marchi et al. (2011) and Sabbi et al. (2012), our data are generally much deeper than the others in the literature and, therefore, more sensitive to older activity. Indeed, our prediction about the beginning of activity in NGC 2070, about 20 Myr ago, is only accessible with our data. Moreover, our analysis implements the PARSEC evolutionary models, which cover consistently the entire evolution from the PMS phase to the post-MS phase, whereas all previous analyses had been forced to combine models for the PMS phase (Siess et al. 2000; Tognelli et al. 2011) and other models for later phases.

Despite these differences, our SFH is broadly consistent with the aforementioned results. Of particular interest is the 7 Myr epoch, when our solution predicts a significant SF enhancement. This event is generally consistent with, or slightly older than, what is found in all other studies. Similarly to De Marchi et al. (2011), we find evidence of some activity prior to 10 Myr ago, whose rate is, at most, one order of magnitude lower than the recent one.

From a spatial point of view, the activity shifts to younger ages in moving from our subregion A1 to A3, resembling the inward progression found by Selman et al. (1999). This is interesting, given that Selman et al. (1999) and this work use complementary mass ranges, above 20 $M_\odot$ in the case of Selman et al. (1999) and below 7 $M_\odot$ in our case. The inward scenario is also broadly consistent with the De Marchi et al. (2011), Walborn & Blades (1997), and Sabbi et al. (2012) findings. De Marchi et al. (2011) found that stars younger than 4 Myr are more concentrated toward R136 than stars older than 12 Myr. These authors also found a remarkable lack of old activity (>12 Myr) near R136, whereas the old component is not significantly different in our subregions. However, the data in our subregions A2 and A3 are not deep enough to allow for a conclusive argument.

7.2. Reddening

Our results predict that stars younger and older than about 10 Myr are on average reddened by $E(B-V) \sim 0.4 \pm 0.05$ and $\sim 0.6 \pm 0.1$, respectively. Because young stars are spatially more concentrated, this also translates into a negative reddening gradient toward the center. This trend is in apparent contrast to the findings of Zaritsky (1999), who found that the young populations (star-forming regions a few megayears old) in the LMC are more reddened than the older ones (>1 Gyr). However, we point out that the timescales here are much shorter; our "old" population is only a few megayears older than the young one. Besides, all results indicate a large reddening dispersion (at least 0.1 mag).

Looking at the literature, we find a general consensus for highly variable reddening in the NGC 2070 neighborhood.

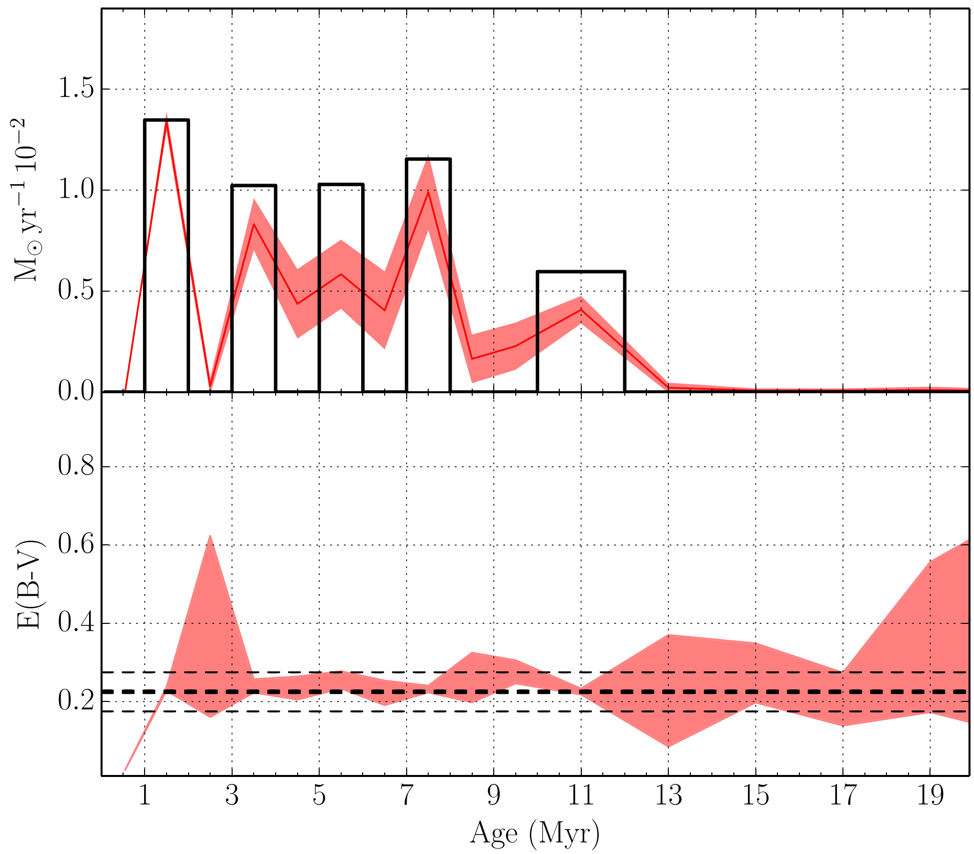

Figure 22. SFH recovery test. The top panel shows the SFH (input in black, recovered in red), and the bottom panel shows the $E(B-V)$ (input in black, recovered in red).

More specifically, De Marchi & Panagia (2014) used UMS and RC stars to study extinction around NGC 2070. Once corrected for the foreground contribution ($E(B-V) = 0.07$), our average prediction for the young component is very close to the peak of their reddening distribution obtained from UMS stars (see the blue histogram in their Figure 9), while our average prediction for the old component is well within their reddening dispersion.

Our reddening for the young population is also in good agreement with the results of Selman et al. (1999). These authors used stars more massive than 20 $M_{\odot}$ and found average extinctions in the range $A_V = 1.1$–1.5 ($E(B-V) = 0.35$–0.5).

8. COMPARISON WITH OTHER STARBURST REGIONS

Within the MW, a smaller analog of NGC 2070 can be found in the Carina Nebula, a massive star-forming region of $(4-6) \times 10^4\,M_{\odot}$ (Smith & Brooks 2007), harboring over 70 O-type stars spread across a region of $\sim$30 pc. Using the Infrared Array Camera on board the *Spitzer Space Telescope*, Smith et al. (2010) studied the population of young stellar objects and inferred a roughly constant SF rate over the past $\sim$3 Myr.

Outside the MW, NGC 346 (33 O-type stars; Massey et al. 1989), the largest star-forming region in the Small Magellanic Cloud, shows similarities with the overall history of NGC 2070. NGC 346 started to form stars about 6–8 Myr ago and peaked about 3 Myr ago before dropping to a lower level (see Cignoni et al. 2011). If we exclude R136, which is ten times more active than NGC 346, even the peak rate per pc^2 of region A3 is similar or only slightly higher than the peak rate in NGC 346 (about $2 \times 10^{-5}\,M_{\odot}\,\mathrm{yr^{-1}\,pc^{-2}}$ between 4 and 5 Myr ago; Cignoni et al. 2011).

In the nearby Scd galaxy M33, with a size of 265 pc, the giant H II region NGC 604 ($\approx$200 O-type stars; Hunter et al. 1996a) exceeds the size of 30 Doradus, but shows a concentration of massive stars 10–100 times lower than R136 (Hunter et al. 1996a). Using spectral energy distribution fitting based on NICMOS/*HST* photometry, Eldridge and Relaño (2011) identified two distinct stellar populations with average ages 3.2 ± 1.0 and 12.4 ± 2.1 Myr, respectively. The total mass of the young component was estimated to be around $3.8 \times 10^5\,M_{\odot}$. Using spectral and photometric data from the *Spitzer* and *Herschel* Space Telescopes, Martínez-Galarza et al. (2012) recovered an average age of 4 ± 1 Myr and a total mass around $1.6 \times 10^5\,M_{\odot}$.

9. CONCLUSIONS

We have presented a detailed analysis of the SF history in the NGC 2070 star-forming region, located in the heart of 30 Doradus in the LMC, using deep optical and NIR CMDs from the HTTP. We used a new synthetic CMD approach combined with the latest Padova models (PARSEC), the first to cover homogeneously all stellar phases from PMS to post-MS.

In our implementation we encountered a number of interesting challenges. We summarize here our main conclusions:

SFH: we found that NGC 2070 experienced prolonged activity, starting at least 7 Myr ago. We identify three major events in the history of this star-forming region:

1. ≈20 Myr ago: This epoch demarcates the commencement of the first significant period of SF. Prior to this epoch, local activity is not distinguishable from the average activity in the LMC field.
2. 7 Myr ago: The SF accelerated throughout the entire region.
3. 1–3 Myr ago: The activity reached a peak. In this time range, the SF moves from the periphery to the central regions. Our innermost subregion (A3) shows a maximum activity 1–2 Myr ago.

Stellar mass: We estimate the stellar mass of NGC 2070 out of 20 pc to be $\approx 8.7 \times 10^4\, M_\odot$.

Reddening: Concerning the reddening distribution, we find an average $E(B-V) \approx 0.4$ mag for the young population (<10 Myr old), and ≈0.6 mag for the old one (>10 Myr old). An explanation could be that only in the last few megayears has the SF been vigorous enough to sweep away part of the gas through stellar winds. Another possibility is that the old activity took place on the far side of the NGC 2070 nebula as seen from us, so those stars experience most of the line-of-sight optical depth.

IMF: Except in the innermost few parsecs, where the incompleteness is too severe to allow firm conclusions, a Kroupa IMF in the range 0.5–7 $M_\odot$ is compatible with the data. This corroborates and extends the result of Andersen et al. (2009) to subsolar masses. To the level we can measure, low-mass stars can form in starburst regions in the same way they form in low-density environments. At high masses, our synthetic CMDs tend to underestimate the star counts in the densest regions. This may suggest a flattening of the IMF above 10 $M_\odot$.

We would like to thank Mario Gennaro, Nino Panagia, Martha Boyer, Chris Evans, Jay Gallagher, Karl Gordon, Anton Koekemoer, Soren Larsen, and Selma de Mink for helpful comments, discussions, and contributions to other aspects of HTTP. E. K. G. gratefully acknowledges funding via the Collaborative Research Center "The Milky Way System" (SFB881) of the German Research Foundation (DFG), particularly via subproject B5. M. T. has been partially funded by the Italian PRIN-MIUR grant 2010LY5N2T. D. A. G. kindly acknowledges financial support by the German Research Foundation (DFG) through grant GO 1659/3-2. Support for program #12939 was provided by NASA to the US team members through a grant from the Space Telescope Science Institute, which is operated by AURA, Inc., under NASA contract NAS 5-26555.

APPENDIX

As done previously (Cignoni et al. 2006, 2011), we parameterize the synthetic CMD as a linear superposition of basic CMDs generated with step-function-like SF, metallicity, and reddening. In the specific case of this paper, we deal with a grid of 18 steps in age (plus one parameter controlling field contamination) and 20 steps in reddening, for a total of 380 parameters. To explore this wide parameter space, we have combined a well-tested genetic algorithm (GA), Pikaia[18], with a local search routine. As shown in various papers (see, e.g., Ng et al. 2002; Aparicio & Hidalgo 2009; Small et al. 2013), GAs allow us to find a global optimum more efficiently than a local search alone. In our approach, the synergy of the GA and a local search combines the advantages of both worlds. In the next sections we describe the synthetic population code and the optimization routine (GA + local search). Finally, the capabilities of the approach are tested with artificial data.

A.1 Synthetic CMDs

The basic synthetic CMDs(j, k) are populated through the following Monte Carlo procedure: (1) synthetic masses and ages are extracted from the assumed IMF and the jth SF step, respectively; and (2) synthetic masses and ages are converted to absolute synthetic magnitudes and colors by using a fine grid of isochrones. For our calculations we used the latest (V.1.2S) PARSEC isochrones, covering the entire mass spectrum of 0.1–350 $M_\odot$ from the PMS phase to the early-AGB phase. (3) A fraction q of synthetic stars is randomly chosen to have a companion. The masses of companions are extracted from the same IMF and their flux is added to the flux of the primaries. (4) The absolute synthetic photometry is put at the distance of the LMC and reddened with the kth reddening. To produce realistic simulations, all basic CMDs are degraded with photometric errors and incompleteness, as estimated from artificial-star tests (see Section 5.2).

To have all stellar phases well populated, the synthetic CMDs are generated with a large number of stars (10^6). Once constructed, the basic CMDs(j, k) are binned in n bins of color and m bins of magnitude. The final result is a library of $j \times k$ 2D histograms CMD$_{m,n}(j, k)$, and any CMD can be expressed as a linear combination of these two-dimensional histograms (see Equation (1)). The coefficients $S(j, k)$ that multiply each of the CMD$_{m,n}(j, k)$ are the SF rate at the time step j and reddening step k. The sum over j and k of $S(j, k) \times$ CMD$_{m,n}(j, k)$ provides the total star counts $N_{m,n}$ predicted in the CMD bin (m, n) by the SF $S(j,k)$:

$$N_{m,n} = \sum_{j,k} \left[S(j, k) \times \mathrm{CMD}_{m,n}(j, k) \right]. \tag{1}$$

Including the reference field in the models corresponds to changing Equation (1) into (2):

$$N_{m,n} = \sum_{j,k} \left[S(j, k) \times \mathrm{CMD}_{m,n}(j, k) \right] + S_F(k) \times F_{m,n}(k)] \tag{2}$$

where $S_F(k)$ regulates the number of field stars with kth reddening, while $F_{m,n}(k)$ is the actual number of stars in the reference field (reddened with the kth reddening) in the CMD bin (m, n).

A.2 Best Solution Search

Once the observational CMD is binned as well, the next step is to search for the combination of basic CMDs that minimizes the CMD residuals between data and model. For this task we implemented a likelihood distance, whose minimization is not biased by low count statistics. The combination of basic CMDs

[18] Routine developed at the High Altitude Observatory and available in the public domain: http://www.hao.ucar.edu/modeling/pikaia.php.

that minimizes the likelihood corresponds to the most likely SFH behind the data. The uncertainty around the recovered best solution will be the sum in quadrature of a statistical error, obtained through a data bootstrap, and a systematic error, obtained by rederiving the SFH using different age binnings and CMD binning.

In our approach, the likelihood is minimized with an HGA, which combines a classical GA with a local search. Pure GAs are iterative probabilistic algorithms for solving a problem that mimic processes found in natural biological evolution. Compared to local search algorithms, GAs explore the search space in more points simultaneously, so they are far less sensitive to the initial conditions and show remarkable ability to escape from local minima. Shortcomings of GAs are the weak ability for local exploration and the slow convergence rate. The proposed HGA aims to overcome both by alternating two phases: a GA, whose goal is to search for a quasi-global solution, and a local search, whose goal is to increase solution accuracy. The synergy of the two incorporates the exploration ability of GAs and the exploitation ability of the local search algorithm. For this study we implemented both *parallel* and *serial* hybridization. The parallel one is applied to each iteration and aims to enhance offspring likelihood by means of a local search before moving to the next generation. The serial one consists of applying a final local search, after which the GA population has evolved to the region containing the global solution.

A.3 Test

To test our approach, we have generated synthetic data with features resembling NGC 2070 (10,000 stars brighter than $F555W = 24$). To simulate the observational conditions, this fake population is convolved with photometric uncertainties and incompleteness from the artificial star tests of NGC 2070. The input SFH is a sequence of five bursts of different ages and duration 1 Myr, and the input reddening distribution is built with 50% of the stars with $E(B-V)$ between 0.20 and 0.25, 25% between 0.25 and 0.30, and 25% between 0.15 and 0.20. Figure 22 shows the result of the reconstruction. The input SFH and reddening distribution are in black; the best reconstructed counterparts are in red. The recovered SFH looks like a smoothed version of the input SFH, due to the finite time resolution associated with the discrete nature of the data and the ill-conditioned nature of mathematical inverse problems. However, overall, input functions are successfully recovered, with most of the differences within the uncertainties. Moreover, a bursty SFH is recovered more accurately if the time gap between the individual bursts is longer.

REFERENCES

Andersen, M., Zinnecker, H., Moneti, A., et al. 2009, ApJ, 707, 1347
Anderson, A., & King, J. R. 2006, STSCI Inst. Sci. Rep. ACS 2006-01 (Baltimore: STScI)
Anderson, J., Sarajedini, A., Bedin, L. R., et al. 2008, AJ, 135, 2055
Aparicio, A., & Hidalgo, S. L. 2009, AJ, 138, 558
Maíz Apellániz, J., Evans, C. J., Barbá, R. H., et al. 2014, A&A, 564, A63
Baraffe, I., Chabrier, G., Allard, F., & Hauschildt, P. H. 2002, A&A, 382, 563
Baraffe, I., Chabrier, G., & Gallardo, J. 2009, ApJL, 702, L27
Baume, G., Vázquez, R. A., Carraro, G., & Feinstein, A. 2003, A&A, 402, 549
Belikov, A. N., Hirte, S., Meusinger, H., Piskunov, A. E., & Schilbach, E. 1998, A&A, 332, 575
Bosch, G., Selman, F., Melnick, J., & Terlevich, R. 2001, A&A, 380, 137
Brandl, B., Sams, B. J., Bertoldi, F., et al. 1996, ApJ, 466, 254
Brandner, W., Grebel, E. K., Barbá, R. H., Walborn, N. R., & Moneti, A. 2001, AJ, 122, 858
Bressan, A., Marigo, P., Girardi, L., et al. 2012, MNRAS, 427, 127
Carrera, R., Gallart, C., Aparicio, A., & Hardy, E. 2011, AJ, 142, 61
Castellani, V., Degl'Innocenti, S., Girardi, L., et al. 2000, A&A, 354, 150
Cignoni, M., Degl'Innocenti, S., Prada Moroni, P., & Shore, S. N. 2006, A&A, 459, 783
Cignoni, M., & Tosi, M. 2010, Dwarf Galaxies and Cosmology, AdAst, 2010, 158568
Cignoni, M., Tosi, M., Sabbi, E., et al. 2010, ApJL, 712, L63
Cignoni, M., Tosi, M., Sabbi, E., Nota, A., & Gallagher, J. S. 2011, AJ, 141, 31
De Marchi, G., & Panagia, N. 2014, MNRAS, 445, 93
De Marchi, G., Panagia, N., & Girardi, L. 2014, MNRAS, 438, 513
De Marchi, G., Paresce, F., Panagia, N., et al. 2011, ApJ, 739, 27
de Mink, S. E., Brott, I., Cantiello, M., et al. 2012, in ASP Conf. Ser. 465, Proc. Scientific Meeting in Honor of Anthony F. J. Moffat, ed. L. Drissen et al. (San Francisco, CA: ASP), 65
Doran, E. I., Crowther, P. A., de Koter, A., et al. 2013, A&A, 558, A134
Eldridge, J. J., & Relaño, M. 2011, MNRAS, 411, 235
Espinoza, P., Selman, F. J., & Melnick, J. 2009, A&A, 501, 563
Fitzpatrick, E. L., & Massa, D. 1999, ApJ, 525, 1011
Fitzpatrick, E. L., & Savage, B. D. 1984, ApJ, 279, 578
González Delgado, R. M., Leitherer, C., Heckman, T., & Cerviño, M. 1997, ApJ, 483, 705
Gouliermis, D. A. 2012, SSRv, 169, 1
Gouliermis, D. A., Dolphin, A. E., Brandner, W., & Henning, T. 2006, ApJS, 166, 549
Grebel, E. K., & Chu, Y.-H. 2000, AJ, 111, 787
Greissl, J., Meyer, M. R., Christopher, M. H., & Scoville, N. Z. 2010, ApJ, 710, 1746
Grocholski, A. J., van der Marel, R. P., Aloisi, A., et al. 2012, AJ, 143, 117
Harris, J., & Zaritsky, D. 1999, AJ, 117, 2831
Haschke, R., Grebel, E. K., & Duffau, S. 2011, AJ, 141, 158
Hénault-Brunet, V., Evans, C. J., Sana, H., et al. 2012, A&A, 546, AA73
Hosokawa, T., Offner, S. S. R., & Krumholz, M. R. 2011, ApJ, 738, 140
Hußmann, B., Stolte, A., Brandner, W., Gennaro, M., & Liermann, A. 2012, A&A, 540, A57
Hunter, D. A., Baum, W. A., O'Neil, E. J., Jr., & Lynds, R. 1996a, ApJ, 456, 174
Hunter, D. A., O'Neil, E. J., Jr., Lynds, R., et al. 1996b, ApJL, 459, L27
Hunter, D. A., Shaya, E. J., Holtzman, J. A., et al. 1995, ApJ, 448, 179
Hyland, A. R., Straw, S., Jones, T. J., & Gatley, I. 1992, MNRAS, 257, 391
Kennicutt, R. C., Jr. 1991, The Magellanic Clouds, Vol. 148 (Dordrecht: Kluwer Academic Publishers)
Kroupa, P. 2001, MNRAS, 322, 231
Luck, R. E., Moffett, T. J., Barnes, T. G., III, & Gieren, W. P. 1998, AJ, 115, 605
Macri, L. M., Stanek, K. Z., Bersier, D., Greenhill, L. J., & Reid, M. J. 2006, ApJ, 652, 1133
Marigo, P., Girardi, L., Bressan, A., et al. 2008, A&A, 482, 883
Martínez-Galarza, J. R., Hunter, D., Groves, B., & Brandl, B. 2012, ApJ, 761, 3
Massey, P., & Hunter, D. A. 1998, ApJ, 493, 180
Massey, P., Parker, J. W., & Garmany, C. D. 1989, AJ, 98, 1305
Mayne, N. J. 2010, MNRAS, 408, 1409
Ng, Y. K., Brogt, E., Chiosi, C., & Bertelli, G. 2002, A&A, 392, 1129
Panagia, N., Gilmozzi, R., Macchetto, F., Adorf, H.-M., & Kirshner, R. P. 1991, ApJL, 380, L23
Pietrzyński, G., Graczyk, D., Gieren, W., et al. 2013, Natur, 495, 76
Rubio, M., Barbá, R. H., Walborn, N. R., et al. 1998, AJ, 116, 1708
Rubio, M., Roth, M., & Garcia, J. 1992, A&A, 261, L29
Sabbi, E., Anderson, J., Lennon, D. J., et al. 2013, AJ, 146, 53
Sabbi, E., Lennon, D. J., Gieles, M., et al. 2012, ApJL, 754, LL37
Sabbi, E., Lennon, D. J., Anderson, J., et al. 2015, ApJS, submitted
Sana, H., de Koter, A., de Mink, S. E., et al. 2013, A&A, 550, AA107
Schaefer, B. E. 2008, AJ, 135, 1
Selman, F., Melnick, J., Bosch, G., & Terlevich, R. 1999, A&A, 347, 532
Siess, L., Dufour, E., & Forestini, M. 2000, A&A, 358, 593
Sirianni, M., Nota, A., Leitherer, C., De Marchi, G., & Clampin, M. 2000, ApJ, 533, 203
Small, E. E., Bersier, D., & Salaris, M. 2013, MNRAS, 428, 763
Smith, N., & Brooks, K. J. 2007, MNRAS, 379, 1279
Smith, N., Povich, M. S., Whitney, B. A., et al. 2010, MNRAS, 406, 952
Soderblom, D. R., Hillenbrand, L. A., Jeffries, R. D., Mamajek, E. E., & Naylor, T. 2014, in Protostars and Planets VI, ed. H. Beuther et al. (Tucson, AZ: Univ. Arizona Press), 219
Stauffer, J. R. 1980, AJ, 85, 1341

Stolte, A., Brandner, W., Brandl, B., Zinnecker, H., & Grebel, E. K. 2004, AJ, 128, 765
Tang, J., Bressan, A., Rosenfield, P., et al. 2014, MNRAS, 445, 4287
Tognelli, E., Prada Moroni, P. G., & Degl'Innocenti, S. 2011, A&A, 533, 109
Tolstoy, E., Hill, V., & Tosi, M. 2009, ARA&A, 47, 371
Tosi, M., Greggio, L., Marconi, G., & Focardi, P. 1991, AJ, 102, 951
Walborn, N. R., Barbá, R. H., Brandner, W., et al. 1999, AJ, 117, 225
Walborn, N. R., & Blades, J. C. 1997, ApJS, 112, 457
Whitmore, B. C., Zhang, Q., Leitherer, C., et al. 1999, AJ, 118, 1551
Zaritsky, D. 1999, AJ, 118, 2824